Transit-amplifying cells coordinate changes in intestinal epithelial cell-type composition

Laura E. Sanman[1]†, Ina W. Chen[1]†, Jake M. Bieber[1,2], Veronica Steri[3,4], Byron Hann[3,4], Lani F. Wu[1]*, Steven J. Altschuler[1]*

[1]Department of Pharmaceutical Chemistry, University of California San Francisco, San Francisco, CA 94158, USA

[2]Graduate Program in Bioengineering, University of California Berkeley, University of California San Francisco, San Francisco CA 94158, USA

[3]Helen Diller Family Comprehensive Cancer Center, University of California, San Francisco, San Francisco, CA 94158, USA.

[4]Preclinical Therapeutics Core, University of California, San Francisco, San Francisco, CA 94158, USA.

*Correspondence to: lani.wu@ucsf.edu, steven.altschuler@ucsf.edu

†Equal contributions

Abstract

Renewing tissues have the remarkable ability to continually produce both proliferative progenitor and specialized differentiated cell-types. How are complex milieus of microenvironmental signals interpreted to coordinate tissue cell-type composition? Here, we develop a high-throughput approach that combines organoid technology and quantitative imaging to address this question in the context of the intestinal epithelium. Using this approach, we comprehensively survey enteroid responses to individual and paired perturbations to eight epithelial signaling pathways. We uncover culture conditions that enrich for specific cell-types, including Lgr5^{+} stem and enteroendocrine cells. We analyze interactions between perturbations and dissect mechanisms underlying an unexpected mutual antagonism between EGFR and IL-4 signals. Finally, we show that, across diverse perturbations, modulating proliferation of transit-amplifying cells also consistently changes the composition of differentiated secretory and absorptive cell-types. This property is conserved *in vivo* and can arise from differential amplification of secretory and absorptive progenitor cells. Taken together, the observations highlight an underappreciated role for transit-amplifying cells in which proliferation of these short-lived progenitors provides a lineage-based mechanism for tuning differentiated cell-type composition.

Introduction

A central question in the study of complex tissues is how diverse signals are integrated to regulate cell-type composition. Dissection of mechanisms underlying the mapping from signals to tissue composition is complicated by the heterogeneous makeup of interconnected cell-types, which exert influences upon one another through the lineage structure and cell-cell interactions. Further, most studies focus on the effects of individual signals on individual cell-types, due to a lack of methods that enable systematic identification of signal integration mechanisms. What are the tissue-wide effects of common microenvironmental signals on cell-type composition? How do multiple signals modify each other's effects? Finally, are there intrinsic tissue properties that shape response to diverse signals?

Here, we address these questions in the context of the intestinal epithelium, a model renewing tissue (Beumer & Clevers, 2016; Cheng & Leblond, 1974b; A. Tian et al., 2016). The intestinal epithelium is particularly remarkable in that it maintains a stereotypic tissue composition despite a rapid 3- to 5-day turnover. During renewal of the intestinal epithelium, Lgr5^{+} crypt-base stem cells differentiate into proliferating transit-amplifying (TA) progenitors, which in turn adopt absorptive (enterocyte) or secretory (Paneth, goblet, enteroendocrine (EE)) cell fates (Cheng & Leblond, 1974b) (Figure 1A). The confluence of proliferating and differentiation decision processes establishes tissue composition, which guides overall tissue function. Though much progress has been made in defining the 'parts list' of factors that guide intestinal epithelial renewal (Clevers, 2013; Flier et al., 2009; Yin et al., 2014a), it is unclear how these factors are integrated by the tissue during maintenance and in response to perturbations.

66 To quantitatively measure intestinal epithelial cell-type composition and study its changes in
67 response to microenvironmental signals, we utilized a recently established enteroid monolayer
68 culture system that recapitulates key features of the intestinal epithelium (Thorne et al., 2018).
69 Enteroid monolayer cultures maintain characteristics of intestinal epithelial architecture, including
70 organization into crypt- and villus-like compartments and apical-basolateral polarization.
71 Importantly, these cultures also preserve core tissue processes *ex vivo*, generating all major
72 intestinal epithelial cell-types (Lgr5^{+} stem, TA, and differentiated secretory and absorptive cells)
73 with a turn-over rate similar to the *in vivo* renewal rate. Crucially, due to their 2D nature, enteroid
74 monolayer cultures are amenable to high-throughput screening of perturbations in microwell
75 format. In this work, enteroid monolayers are used as a primary platform for hypothesis generation
76 with key observations further evaluated in 3D organoids and *in vivo*.

77 Here, we present a systems approach for investigating signal integration and lineage processes in
78 the intestinal epithelium. We first expanded the capabilities of the enteroid monolayer platform to
79 monitor and quantify major intestinal epithelial cell-types, such as stem, TA, and differentiated
80 cell-types, in a robust and automated manner. This enabled confirmation of relevant stem and TA
81 functions, such as proliferation and production of differentiated cell-types, in enteroid monolayer
82 cultures. We then combined enteroid culture with high-throughput combinatorial perturbations to
83 profile responses to a diverse set of treatment conditions. Analysis of tissue response profiles
84 identified conditions that enrich for specific intestinal epithelial cell-types and revealed
85 interactions in the integration of perturbations. Finally, studies using enteroid monolayers, 3D
86 organoids, and mice uncovered a global trend in how intestinal epithelial cell-type composition
87 changes in response to perturbations; specifically, a link between TA proliferation and secretory
88 cell composition. Based on experimental observations and mathematical modeling, we propose a

89 model of intestinal epithelial lineage control in which differential amplification of TA progenitors
90 allows the balance of secretory to absorptive cell lineages to be regulated through TA proliferation.

91 **Results**

92 **A quantitative microscopy platform to study regulation of intestinal cell-type composition**

93 As an experimental model for the study of intestinal epithelial cell-type composition in high-
94 throughput, enteroid monolayers should be quantifiable, reproducible, and faithfully recapitulate
95 relevant *in vivo* tissue properties. Here, we develop and test these features of the enteroid
96 monolayer platform.

97 To measure intestinal epithelial composition in high-throughput, we established a computational
98 pipeline to automatically quantify major intestinal cell-types from images of enteroid monolayers
99 (Figure 1B). Specifically, we developed algorithms to detect cells expressing markers for stem
100 ($Lgr5^+$), proliferating (EdU^+), Paneth (Lyz^+), goblet ($Muc2^+$), and enteroendocrine (EE; $ChgA^+$)
101 cells as well as identifying cell nuclei (Hoechst) (Figure 1-Supplement 1, Materials and Methods).
102 Enterocytes were not directly quantified because we were not able to identify a reliable antibody
103 to specifically label this population in immunofluorescence assays. Thus, our studies of
104 differentiated cell-types were limited to the secretory lineage. When evaluated against expert
105 manual counting, the algorithms exhibited high quantification accuracy across the cell-types
106 measured (Table 1).

107 To evaluate reproducibility, cell-type measurements were quantified across replicate wells. A crypt
108 seeding density (10-20% initial confluency) was identified where there was no relationship
109 between initial seeding density and cell-type composition after 48 hours of culture. In this regime,

110 there was also relatively low inter-replicate variability in cell-type numbers. (Figure 1-Supplement
111 2).

112 To assess recapitulation of relevant *in vivo* intestinal epithelial properties, we examined cell-type
113 composition and progenitor cell functions including proliferation and differentiation. We first
114 observed that jejunal enteroid monolayers exhibited cell-type composition comparable to the
115 composition of *in vivo* jejunal epithelium (Table 2). We then confirmed that enteroid monolayers
116 recapitulate progenitor proliferation and production of differentiated cell-types. By labeling
117 cycling cells with EdU upon initial plating, we observed that the initial population of ~25%
118 proliferative (EdU^+) cells produce the vast majority (~80%) of cells in enteroid monolayers after
119 48 hours of culture (Figure 1C). This indicated that the majority of quantified cells after 48 hours
120 of culture were produced by initial progenitors. Further, we observed EdU^+ cells that colocalized
121 with markers of Paneth (Lyz), goblet (Muc2), and EE (ChgA) cells, indicating that progenitor cells
122 produce major differentiated cell-types over the 48-hour culture period (Figure 1D).

123 Taken together, enteroid monolayers preserve important characteristics of the intestinal epithelium
124 *ex vivo*, such as cell-type composition and production of differentiated cell-types. Enteroid
125 monolayers also demonstrate reproducible outgrowth and low replicate variance. Thus, enteroid
126 monolayers constitute a robust platform for capturing tissue-wide responses to perturbations and
127 for generating hypotheses on control of intestinal epithelial cell-type composition.

128 **Systematic survey of cell-type composition changes in response to single and pairwise**
129 **signaling modulators**

130 To map a wide range of tissue composition phenotypes, 13 epithelial-intrinsic and
131 microenvironmental modulators that target eight core intestinal epithelial signaling pathways
132 (Wnt, BMP, Notch, HDAC, JAK, p38MAPK, TGF-beta, EGFR (Basak et al., 2017a; Batlle et al.,

133 2002; Mathieu Houde et al., 2001; Richmond et al., 2018a; Rodríguez-Colman et al., 2017; van
134 der Flier & Clevers, 2009; Yin et al., 2014b)) and are known to have diverse effects on tissue cell-
135 type composition were selected (Table 3). In previous reports, combinations of perturbations have
136 been shown to be more effective than single perturbations in enriching particular cell-types (Basak
137 et al., 2017a; Yin et al., 2014b). Thus, to survey a broad range of tissue states, modulators were
138 applied to enteroid monolayers individually (13 conditions) and in all possible pairwise
139 combinations (78 conditions) (workflow: Figure 2-Supplement 1A). Perturbation concentrations
140 were guided by literature reports and confirmed with dose-response experiments (Table 3, Figure
141 2-Supplement 1B) (Basak et al., 2017a; von Moltke et al., 2015; Yin et al., 2014b).

142 We then sought to combine cell-type number measurements into readouts that reflect changes in
143 important aspects of intestinal epithelial cell-type composition. Changes in overall tissue
144 composition can be attributed to a number of changes in underlying cell-type populations. For
145 instance, an overall decrease in the fraction of a specific cell-type, such as goblet cells, may be
146 caused by an increase in the number of progenitors (or other cell-types), a decrease in the secretory
147 fraction in the differentiated cell population, or a decrease in goblet cells within the secretory cell
148 lineage. To distinguish between these different possibilities, we designed features that measured
149 the size of the progenitor population as well as the relative composition of cells in the differentiated
150 population, as follows.

151 To quantify changes in the progenitor cell populations, we measured the absolute numbers of
152 proliferating stem (EdU^+ $Lgr5^+$) and TA (EdU^+ $Lgr5^-$) cells (Figure 2A, Figure 2-Supplement 2A).
153 Since specific TA markers are lacking, TA cells were defined as non-stem proliferating cells. To
154 quantify changes in the relative makeup of the differentiated population, we designed fractional
155 readouts that reflect changes in two differentiation branching points: the secretory-absorptive

156 branch point, and the secretory cell-type branch point. To capture secretory vs. absorptive lineage
157 biases, we computed the fraction of differentiated ($Lgr5^-$ EdU^-) cells that express secretory
158 (Paneth+goblet+EE) markers (#secretory/#diff) (Figure 2A, Figure 2-Supplement 2B). The sum
159 of Paneth, goblet, and EE cells is a reasonable approximation for the number of secretory cells as
160 these cell-types make up the majority of secretory cells (Cheng & Leblond, 1974b; Haber et al.,
161 2017). Finally, to capture biases towards different cell-types within the secretory lineages, we
162 computed the specific fractions of all secretory cells positive for Paneth (Lyz), goblet (Muc2), and
163 EE (ChgA) cell markers (#Paneth/#secretory, #goblet/#secretory, #EE/#secretory) (Figure 2A,
164 Figure 2-Supplement 2C).

165 After treatment with established modulators of cell-type composition (GSK3-i+HDAC-i, Notch-i,
166 IL-4, EGFR-i, PORCN-i), changes in enteroid monolayer cell-type readouts were in agreement
167 with previous 3D organoid and *in vivo* studies (Basak et al., 2017a; Beumer & Clevers, 2016; Qi
168 et al., 2017; van Es et al., 2005; von Moltke et al., 2015; Yin et al., 2014b) (Figure 2-Supplement
169 3A, Table 3). Changes in the prevalence of each cell-type were also confirmed at the RNA level
170 using quantitative reverse transcription PCR (qRT-PCR; Figure 2-Supplement 3B).

171 **Identification of conditions that enrich for $Lgr5^+$ stem and EE cells**

172 Single and pairwise perturbation effects on intestinal epithelial cell-type composition (546
173 measurements = 91 conditions x 6 cell-type readouts) were measured (Figure 2B). The vast
174 majority of measurements were previously uncharacterized, with a number of conditions strongly
175 modulating different aspects of tissue composition (Table 4). Below, we highlight conditions that
176 were previously unknown to enrich for stem and EE cells.

177 Pairwise combinations of inhibitors of GSK3, p38MAPK, BMPR, HDAC, and JAK1/2 increased
178 the number of $Lgr5^+$ stem cells (Figure 2B, bottom callout 1). Notably, these conditions caused

179 similar, if not increased, enrichment for Lgr5$^+$ stem cells compared to the current benchmark
180 condition (GSK3 inhibitor + HDAC inhibitor (Yin et al., 2014a)). Lgr5$^+$ stem cell enrichment was
181 also observed at the RNA level, as indicated by qRT-PCR analysis of Lgr5 RNA (Figure 2C).
182 Since JAK1/2 had not been connected with stemness in the mammalian intestinal epithelium in
183 the absence of inflammation (Richmond et al., 2018b), we repeated the GSK3-i and JAK1/2-i
184 treatment in 3D organoids and again observed expansion of the Lgr5$^+$ stem cell population (Figure
185 2D).

186 Conditions were also identified that selectively enrich for EE cells relative to other secretory cell-
187 types (Table 4). The condition that most strongly enriched for EE cells was the combination of
188 TGF-beta and PORCN inhibitor (Figure 2B, bottom callout 2). TGF-beta and PORCN inhibitor
189 treatment of enteroid monolayers also caused an increase in RNA levels of the EE marker ChgA
190 relative to RNA levels of markers of other secretory cell-types (Figure 2E). Since a connection
191 between TGF-beta signaling and EE cell regulation had not been previously established, we
192 applied the treatment to 3D organoids and again observed EE enrichment (Figure 2F).

193 **Interaction mapping reveals mutual antagonism between IL-4 and EGFR-i**

194 After analyzing perturbations effects individually, we next examined how pairs of perturbations
195 interact to modulate cell-type composition. A commonly used framework for identifying
196 perturbation interactions is a multiplicative model, where the combined effect of two non-
197 interacting perturbations is expected to be the product of the effects of individual perturbations
198 (Dixon et al., 2009). For each cell-type composition readout, we analytically defined an interaction
199 between any pair of perturbations as a combinatorial perturbation effect that deviated strongly
200 (effect size>5) from the expectation of the multiplicative model. (The multiplicative model was
201 chosen due to its interpretability and fit to the data; Figure 3-Supplement 1, Materials and

202 Methods). Biologically, interactions were interpreted as direct or indirect connections between the
203 perturbed signaling pathways (Coster et al., 2017; Papin et al., 2005). The majority of perturbation
204 pairs showed little deviation from the multiplicative model expectation (Figure 3-Supplement 1A).
205 Interestingly, perturbation interactions were predominantly observed in the regulation of EdU^+
206 stem and TA cell numbers, as compared to the regulation of secretory, goblet, Paneth, or EE cell
207 prevalence (Figure 3A).

208 In some cases, identified interactions reflected known pathway biology, such as interactions
209 between perturbations that modulate the same signaling pathway (e.g. the synergistic effect of
210 Wnt3a and GSK3-i, Figure 3-Supplement 2). Other cases were less expected and suggest novel
211 interactions in the regulation of specific cell-types. One particularly unexpected example is the
212 interaction between IL-4 and EGFR-i in regulating TA cells. IL-4 and EGFR-i are not known to
213 interact or utilize a shared signaling pathway and, interestingly, appeared mutually antagonistic in
214 combination. When either IL-4 or EGFR-i was applied singly, the number of TA cells was reduced
215 by ~4 and ~6 log-fold relative to control, respectively. However, when IL-4 and EGFR-i were
216 applied in combination, the number of TA cells was reduced by only ~1.5 log-fold relative to
217 control (Figure 3B).

218 We investigated potential mechanisms for the observed mutual antagonism of IL-4 and EGFR-i.
219 EGFR-i treatment decreases proliferation by reducing MEK-Erk activity (Basak et al., 2017a).
220 However, IL-4 treatment resulted in Erk activation (as measured by phospho-Erk nuclear
221 translocation) even in the context of EGFR inhibition (Figure 3C). This suggested that IL-4
222 antagonized the effects of EGFR-i by bypassing EGFR-i to activate Erk. When IL-4 and EGFR-i
223 were applied in the context of MEK inhibition (which is upstream of Erk), IL-4 did not antagonize
224 the effects of EGFR-i on TA cell numbers (Figure 3-Supplement 3A) or induce phospho-Erk

225 nuclear translocation (Figure 3-Supplement 3B). This indicated that IL-4 activates MEK-Erk
226 signaling upstream of MEK. In the other direction, IL-4 reduced proliferation in both enteroid
227 monolayers and 3D organoids by increasing BMP2 (the epithelial paralog of mesenchymal BMP4
228 (Goldman et al., 2009)) production by the tissue (Figure 3D). The addition of a BMP receptor
229 inhibitor, BMPR-i, rescued the IL-4-induced decrease in transit-amplifying cell numbers further
230 confirming BMP secretion as the mechanism by which IL-4 dampens proliferation (Figure 3-
231 Supplement 4A,B). EGFR-i reduces BMP2 production induced by IL-4 treatment, suggesting a
232 mechanism by which EGFR-i antagonizes the effects of IL-4 (Figure 3E).

233 In summary, analysis of perturbation interactions, which occurred predominantly in progenitor
234 cells, revealed a surprising mutual antagonism between IL-4 and EGFR signaling in the regulation
235 of TA cells. Mechanistic investigation revealed that the mutual antagonism arises from IL-4
236 bypassing EGFR-i-induced blockade of MEK-Erk-driven cell cycle progression and EGFR-i
237 blocking IL-4-induced production of antiproliferative BMP2.

238 **Modulating transit-amplifying cell proliferation alters secretory cell-type composition**

239 In addition to gaining insights into the signaling regulation of tissue composition, we applied this
240 dataset to survey global trends in how intestinal epithelial cell-type composition changes in
241 response to perturbations. In particular, the observation of increased interaction in regulation of
242 the progenitor populations led us to investigate how changes in progenitor cell numbers relate to
243 changes in the composition of differentiated cell-types. Despite the diversity of perturbation
244 mechanisms, we observed a surprising trend: the numbers of transit-amplifying cells negatively
245 correlated with the fraction of differentiated cells that express secretory markers (Figure 4A) as
246 well as with the fraction of secretory cells that express the EE marker (Figure 4-Supplement 1A).
247 In contrast, little-to-no correlation was observed between the number of proliferating Lgr5^{+} stem

248 cells and differentiated cell-type composition (Figure 4A, Figure 4-Supplement 1A), indicating
249 that the trend was specific for TA cells. To assess whether the cell-type correlations were driven
250 by any individual perturbation, perturbations were dropped one at a time from the dataset
251 (dropping all single and pairwise conditions containing the perturbation) and correlations were re-
252 calculated for each data subset. We found that dropping EGFR-i from the dataset largely abrogated
253 the anticorrelation between TA number and EE fraction (Figure 4-Supplement 1B, red arrowhead),
254 which is consistent with recent work suggesting that EE cell production can be triggered by EGFR-
255 i-induced stem cell quiescence (Basak et al., 2017a). However, the anticorrelation between TA
256 number and secretory fraction is not driven by a specific perturbation (Figure 4B), possibly
257 indicating a tissue-intrinsic property.

258 We further investigated the anticorrelation between TA numbers and secretory cell fraction in
259 enteroid monolayers, 3D organoids, and *in vivo*. To test whether the correlation is driven by TA
260 proliferation, we directly modulated proliferation in enteroid monolayers using Cdk and Aurora
261 kinase inhibitors and found that inhibiting proliferation, which decreases TA numbers, caused an
262 increase in secretory cell fractions (Figure 4C). Further, CDK4/6 inhibition increased the secretory
263 cell fraction (and decreased TA cell numbers) in a dose-dependent manner (Figure 4-Supplement
264 2). We then used 3D organoids to demonstrate that the correlation was specific to TA, and not
265 stem cells. 3D organoid cultures were first enriched for either stem (treatment with GSK3-
266 i+HDAC-i (Yin et al., 2014b)) or TA (treatment with PORCN-i) cells. qRT-PCR analysis
267 confirmed enrichment for Lgr5 RNA over Ki67 RNA in GSK3-i+HDAC-i-treated 3D organoids,
268 and Ki67 RNA over Lgr5 RNA in PORCN-i-treated 3D organoids (Figure 4-Supplement 3). IF
269 staining also showed almost complete conversion to Lgr5^{+} stem cells in GSK3-i+HDAC-i-treated
270 3D organoids, while PORCN-i-treated 3D organoids retained proliferating (EdU^{+}) cells but lost

271 Lgr5$^+$ stem cells (Figure 4D, images). Organoids were then removed from enrichment media and
272 treated with the CDK4/6 inhibitor palbociclib, which significantly impairs proliferation in 3D
273 intestinal organoids (Basak et al., 2017b). Atoh1 and Hes1 RNA levels were measured by qRT-
274 PCR to quantify changes in secretory and absorptive cell fractions, respectively. Strikingly,
275 CDK4/6 inhibition increased the ratio of Atoh1/Hes1 RNA in 3D organoids enriched for TA cells.
276 However, CDK4/6 inhibition had a reduced effect on 3D organoids enriched for Lgr5$^+$ stem cells
277 (Figure 4D, graphs). These data indicate that proliferation of TA cells drives the observed changes
278 in secretory prevalence. Lastly, we validated the correlation between TA proliferation and
279 secretory fraction *in vivo*. Mice (n=8 per group) were treated with the CDK4/6 inhibitor palbociclib
280 or vehicle. After 50 hours of treatment, intestinal crypts were harvested and gene expression was
281 measured by qRT-PCR. CDK4/6-i treatment decreased Ki67 expression, indicating the treatment
282 effectively decreased proliferation (Figure 4-Supplement 4A). Importantly, CDK4/6-i treatment
283 increased the Atoh1/Hes1 ratio (Figure 4E) and, to a lesser extent, the Dll/Notch ratio (Figure 4-
284 Supplement 4B), demonstrating that proliferation is anti-correlated with secretory fraction *in vivo*.

285 **Differential amplification as a model for proliferation-based control of tissue composition**

286 How does altering TA cell proliferation affect the abundance of secretory cells relative to other
287 differentiated (absorptive) cell-types? Previous studies suggest that secretory progenitors are less
288 proliferative compared to absorptive progenitors. In particular, commitment to a secretory fate
289 (specifically expression of the Notch ligand Dll1) has been observed to coincide with cell cycle
290 exit (Stamataki et al., 2011), and lineage tracing experiments found that secretory cell clones are
291 on average smaller than absorptive cell clones (Bjerknes & Cheng, 1999). To experimentally
292 confirm that secretory progenitors indeed undergo fewer divisions than absorptive progenitors, an
293 EdU dilution experiment was conducted. A pulse of EdU was administered for the first 9 hours of

294 culture (less than one TA cell cycle length (Matsu-Ura et al., 2016)), followed by a chase of 39
295 hours (Figure 5A). EdU is initially incorporated into proliferating cells and then subsequently
296 diluted with each cell division. Thus, EdU intensity in differentiated cells serves as a proxy for
297 division number. Cells were fixed and stained for secretory cell markers Lyz, Muc2, and ChgA as
298 well as EdU. EdU intensity distribution for all labeled cells was bimodal, indicating presence of
299 two distinct subpopulations with one population of cells dividing fewer times (higher EdU
300 intensity) than the other population (lower EdU intensity, Figure 5A). The EdU intensity
301 distributions for Lyz^+ Paneth, $Muc2^+$ goblet, and $ChgA^+$ EE cells were clearly shifted right
302 (towards higher EdU intensity) compared to all epithelial cells, indicating that secretory cells
303 divided fewer times compared to the overall population of intestinal epithelial cells (Figure 5A).

304 To mathematically evaluate whether differential amplification of secretory and absorptive
305 progenitors could explain the observed anti-correlation between TA proliferation and secretory
306 cell abundance, a simple exponential growth model was established. We computed the expected
307 number of differentiated progeny cells from progenitor (TA) cells committed to either secretory
308 fates or absorptive fates. The ratio of the expected output from secretory progenitors to that from
309 absorptive progenitors captures the relative prevalence of secretory to absorptive cells in the
310 differentiated population (Materials and Methods). To test how the relative difference in secretory
311 and absorptive progenitor division numbers impacts the relationship between proliferation rate and
312 tissue composition, we scanned through different division rates—and thus division numbers—for
313 secretory and absorptive progenitors. We found that only parameter regimes where secretory
314 progenitors divide fewer times than absorptive progenitors recapitulated the observed anti-
315 correlation between proliferation and the ratio of secretory to absorptive cells (Figure 5B-C, Figure

316 5-Supplement 1). Thus, differential amplification of TA progenitors in the intestinal epithelium
317 could provide a mechanism for controlling secretory-absorptive bias through proliferation.

318 **Discussion**

319 How the intestinal epithelium globally integrates microenvironmental signals to regulate tissue
320 composition has been challenging to study due to a lack of quantitative, high-throughput methods.
321 Here, we developed a platform utilizing enteroid monolayers to comprehensively survey changes
322 in intestinal epithelial cell-type composition to diverse perturbations. This enabled the
323 identification of new culture conditions that enrich for specific cell-types, the dissection of
324 perturbations that have unexpected combined effects on tissue growth, and the discovery that
325 differential amplification of progenitor cells in different lineages can control differentiated cell-
326 type composition. Importantly, recapitulation of perturbation effects and the proliferation-
327 secretory link in both 3D organoids and *in vivo* lends support to the hypothesis generation ability
328 of enteroid monolayers.

329 In terms of specific culture conditions, it was observed that pairwise combinations of GSK3,
330 JAK1/2, HDAC, BMPR, and p38 MAPK inhibitors enriched for Lgr5^{+} stem cells. JAK1/2
331 inhibition has not been connected with regulation of stem cells under non-inflammatory
332 conditions. Intriguingly, during inflammation JAK1/2 is essential for reserve stem cell activation
333 (Richmond et al., 2018a). Since JAK1/2 inhibition increased Lgr5^{+} stem cell numbers, this could
334 indicate a difference in the regulation of homeostatic (Lgr5^{+}) and reserve stem cells. In addition,
335 it was observed that combined TGF-beta stimulation and PORCN inhibition increases the fraction
336 of enteroendocrine cells in the secretory lineage. TGF-beta signaling increases and Wnt signaling
337 decreases as cells migrate up the crypt-villus axis (Barnard et al., 1989; Farin et al., 2016).

338 Therefore, these data suggest a connection between spatial locations on the crypt-villus axis and
339 differentiated cell-type composition.

340 By analyzing combinations of microenvironmental factors, we found more interactions amongst
341 signals regulating progenitor (stem and TA) cell numbers than prevalence of differentiated cell-
342 types. Possible reasons for the increased number of interactions include that either more signals
343 control progenitor proliferation, or that signals act redundantly upon a smaller number of shared
344 pathways. By examining specific pathway interactions, we found an unexpected mutual
345 antagonism between IL-4 and EGFR-i that regulated the TA cell population. It was previously
346 unknown that IL-4 induces BMP production, which has implications for its effects on the intestinal
347 epithelium during type 2 immune responses such as worm infection (von Moltke et al., 2015).
348 Further, it is surprising that IL-4 can bypass EGFR blockade, given recent data suggesting that
349 EGFR is a gatekeeper of MEK-Erk-driven cell cycling in the intestinal epithelium (Basak et al.,
350 2017a).

351 Lastly, our finding that perturbing TA cell proliferation altered the balance of secretory and
352 absorptive differentiated cell-types underpins a new perspective on the role of the intestinal lineage
353 structure in regulating cell-type composition of tissues. Lineage structures have been modeled in
354 the past, such as the branching of progenitors in enabling robust feedback control (Lander et al.,
355 2009). Here, we find that a differential amplification model of transit-amplifying progenitors in
356 different lineages allows for control of tissue cell-type composition through modulation of
357 proliferation. This model can be contrasted with a probabilistic stem cell decision model, in which
358 cell-type composition is determined by stochastic decision-making in stem cells (Balázsi et al.,
359 2011). We do not rule out that probabilistic fate decisions may still play an important role.

360 However, the current study provides evidence that differential amplification of progenitors makes
361 a significant contribution in shaping the tissue composition.

362 The link between TA proliferation and differentiated cell-type composition, as well as the
363 observation of increased perturbation interactions in regulation of TA cells, point to a crucial and
364 currently overlooked role for these short-lived progenitor cells in guiding tissue function. The
365 intestinal epithelium, like many actively renewing tissues, is generated by stem cells that
366 differentiate into short-lived progenitors, such as TA cells, and then assume differentiated cell
367 fates. Intriguingly, many tissues, including skin and the hematopoietic system, feature transit-
368 amplifying cells as intermediates between the stem and differentiated cell populations. By
369 separately processing signals, these short-lived progenitor cell populations may broadly serve as a
370 buffer that enables coordinated tissue responses to changing microenvironments (e.g. worm
371 infections (Birchenough et al., 2016)) while insulating the stem cell population from extreme,
372 transient changes.

373 **Materials and Methods**

374 Mice

375 All animal care and experimentation was conducted under protocol AN-179937 agreed upon by
376 the Administrative Panel on Laboratory Animal Care at the University of California, San
377 Francisco. All our animal studies are performed in full accordance with UCSF Institutional
378 Animal Care and Use Committee (IACUC). 5- to 6-week-old male C57BL/6 mice
379 (C57BL/6NHsd) were purchased from Harlan and housed with ad libitum food and water on a
380 12hr light cycle at the UCSF Preclinical Therapeutics Core vivarium.

381

382 Media

383 Organoid basal media (OBM) consists of Advanced DMEM/F12 with non-essential amino acids
384 and sodium pyruvate (Fisher Scientific #12634-028) containing 1x N-2 (Fisher Scientific
385 #17502-048), 1x B-27 (Invitrogen #17504-044), 10 mM HEPES (Invitrogen #15630080), 1x
386 GlutaMAX (Invitrogen #35050-061), 1 μM N-acetylcysteine (Sigma Aldrich #A9165), 100
387 U/mL penicillin and 100 μg/mL streptomycin (Corning #30-002).
388 For initial seeding, enteroid monolayers were maintained in OBM supplemented with 3 μM
389 CHIR-99021 (Sigma Aldrich #SML1046), 50 ng/mL murine EGF (Invitrogen #PMG8043), 1
390 μM LDN-193189 (Sigma Aldrich #SML0559), 500 ng/mL murine R-spondin-1 (Peprotech
391 #315-32), and 10 μM Y-27632 (Selleck Chemicals #S1049).
392 4 hours after initial seeding, media was changed into OBM supplemented with 50 ng/mL murine
393 EGF, 100 ng/mL murine Noggin, and 500 ng/mL murine R-spondin-1. Perturbations applied in
394 the studies described here were all applied in the background of this medium.

395

396 Enteroid monolayer cultures

397 Enteroid monolayers were derived as previously described (Thorne et al., 2018). Briefly,
398 jejunum was isolated from male mice between 6-12 weeks of age. Mice used were either from
399 the C57BL/6 strain or, when indicated, the Lgr5$^{eGFP\text{-}DTR}$ strain (H. Tian et al., 2011) (kind gift of
400 Frederic de Sauvage, Genentech via Ophir Klein under MTA #OM-216813). Epithelium was
401 released from jejunal tissue by incubation in ice-cold PBS with 3 mM EDTA in PBS (Ambion
402 #9260). Released epithelial tissue was washed 3x with OBM, after which crypts were separated
403 from villus material using 100 and 70 μm cell strainers (BD Falcon) in succession. Crypts were

404 resuspended in seeding media and plated on Matrigel (Thermo Fisher #CB-40234C)-coated 96-
405 well optical bottom plates (BD Biosciences #353219 and Greiner #655090). Typically, 300
406 crypts were seeded per well. We identified this seeding density because, at this density, we did
407 not observe an effect of variations in initial confluency on cell outgrowth (#cells) or cell-type
408 composition (Figure 1-Supplement 2). Four hours after seeding, cells were washed with OBM
409 and incubated in control media containing other perturbations of interest.
410
411 3D organoid cultures
412 3D organoids were cultured as previously described (Sato et al., 2009). For imaging experiments,
413 3D organoids were seeded in 10 μL of Matrigel in 96-well optical bottom plates.
414
415 CDK4/6-i administration to mice and tissue harvest
416 To test the effects of cell cycle inhibition on the secretory:absorptive ratio, palbociclib (LC
417 Laboratories #P-7744) at 150 mg/kg in 50 mM sodium lactate buffer pH 4.4 was administered to
418 mice by oral gavage every 24 hours for 48 hours (at 0 hours, 24 hours, and 48 hours). At 50
419 hours, the small intestine was harvested and intestinal crypts were harvested as described in the
420 enteroid monolayer culture section above. Crypts were lysed in Buffer RLT (RNEasy Kit,
421 Qiagen) for subsequent RNA purification.
422
423 Growth factors and chemical compounds
424 All growth factors and chemical compounds were purchased from suppliers and used as
425 designated without further purification. Unless otherwise indicated, perturbations were used as
426 follows:

Perturbation	Vendor and Catalog #	Concentration
DAPT (Notch-i)	Stemgent #04-0041	10 μM
CHIR-99021 (GSK3-i)	Sigma Aldrich #1046	3 μM
Valproic acid (HDAC-i)	Sigma Aldrich #P4543	1 mM
IWP-2 (PORCN-i)	Selleck Chemicals #S7085	2 μM

Wnt3a	R&D Systems #5036-WN-500	200 ng/mL
TGF-β	PeproTech #100-21C	4 ng/mL
EW-7197 (TGF-βR-i)	Selleck Chemicals #S7530	1 μM
BMP4	R&D Systems #314-BP-010	200 ng/mL
LDN-193189 (BMPR-i)	Sigma Aldrich #SML0559	1 μM
Baricitinib (JAK1/2-i)	Selleck Chemicals #S2851	2 μM
SB202190 (p38MAPK-i)	Sigma Aldrich #S7067	10 μM
IL-4	PeproTech #214-14	20 ng/mL
Erlotinib HCl (EGFR-i)	Selleck Chemicals #S1023	2.5 μM
PD0325901 (MEK-i)	Selleck Chemicals #S1036	1 μM
Palbociclib (PD-0332991) (CDK4/6-i)	Selleck Chemicals #S1116 (organoid studies) or LC Laboratories #-7744 (*in vivo* studies)	10 μM
Flavopiridol (CDK-i)	Selleck Chemicals #S2679	0.3 μM
AT9283 (AuroraK-i)	Selleck Chemicals #S1134	1 μM

427

428 Immunofluorescence assay

429 *Enteroid monolayers:* Enteroid monolayers were washed 1x with warm D-PBS and then fixed
430 with 4% paraformaldehyde in PBS for 15min at room temperature. Cells were then washed with
431 PBS and permeabilized with 0.5% Triton-X-100 in PBS at room temperature for 10min. Cells
432 were washed, blocked with 3% BSA in PBS for 30min, and then incubated in primary antibody
433 in antibody buffer (PBS with 0.3% Triton-X-100, 1% BSA) overnight at 4C. The next day, cells

434 were washed and incubated with secondary antibodies and Hoechst 33342 (5 µg/mL; Invitrogen
435 #H3570) in antibody buffer for 2 hours at room temperature. After this, cells were washed with
436 PBS and imaged in TBS-T (0.1% Tween in 1x TBS pH 7.4).
437 *3D organoids:* Media was carefully aspirated from around Matrigel domes containing 3D
438 organoids using a P100 pipet. 4% paraformaldehyde in PBS was immediately added for 15min at
439 room temperature. Cells were then washed 2x with PBS and permeabilized using 0.5% Triton-X-
440 100 in PBS for 20min at room temperature. Cells were then rinsed 3x10min with 100 mM
441 glycine in PBS with gentle agitation. Cells were blocked in 3% BSA in PBS for 40min and then
442 incubated with primary antibody in antibody buffer overnight at room temperature. The next day,
443 cells were washed 3x20min in antibody buffer and then incubated with fluorescent secondary
444 antibodies and Hoechst in antibody solution for 1hr at room temperature. Cells were then rinsed
445 in PBS and stored and imaged in TBS-T.
446
447 Antibodies
448 All antibodies were purchased from suppliers and used as designated without further
449 purification. Unless otherwise indicated, antibodies were used as follows:

Epitope	**Vendor and Catalog #**	**Dilution**
Lysozyme (Lyz)	Dako	1:2000
Mucin-2 (Muc2)	Santa Cruz Biotechnology #15334	1:100
Chromogranin A (ChgA)	Santa Cruz Biotechnology #393941	1:100
GFP	Abcam #5450	1:2000
Dclk1	Abcam #31704	1:1000
Erk1 (pT202/pY204) + Erk2 (pT185/pY187) (pErk)	Abcam #50011	1:200
Cyclin D1	Life Technologies #MA5-14512	1:200

450

451 EdU pulse and visualization

452 To visualize proliferating cells (specifically, those in S phase), enteroid monolayers were
453 incubated with 10 μM EdU (Thermo Fisher #A10044) in media (containing indicated
454 perturbations or vehicle) for 2 hrs prior to fixation. After immunofluorescence staining, EdU^+
455 cells were visualized using Click chemistry as previously described (Salic & Mitchison, 2008).
456 Briefly, cells were incubated with a reaction mixture containing 1 mM CuSO4 (VWR
457 International #470300-880), 5 μM sulfo-Cyanine5 azide (Lumiprobe #B3330) or 5 μM BDP-FL
458 azide (Lumiprobe #11430), and 100 mM sodium ascorbate (Sigma Aldrich #A4034) in PBS for
459 30min at room temperature.

460

461 Automated brightfield microscopy

462 Upon initial plating, enteroid monolayers were imaged in the brightfield channel using the 10x
463 objective of a Nikon TE200-E epifluorescence microscope. These data were used as a control to
464 determine whether enteroid monolayers were seeded at an optimal and consistent confluency.

465

466 Quantifying % confluency

467 % Confluency (percent of image which is occupied by enteroid monolayer cultures) was
468 quantified from brightfield images using a previously reported algorithm
469 (CellularRegionsFromBrightField function in Supplementary Software 1 from reference
470 (Ramirez et al., 2016)).

471

472 Automated confocal microscopy

473 Enteroid monolayers were imaged on the 10x objective of a Nikon A1 confocal with Ti2-E
474 microscope. The area of each well was covered by 24 individual scans. In each field of view, 4-8
475 z planes were collected at 1024x1024 resolution. Importantly, the nuclear stain was used to
476 autofocus in each new field of view.

477

478 Data availability

479 All data generated or analyzed during this study are included in this published article (and its
480 supplementary information files)

481

482 Immunofluorescence image segmentation and analysis

483 *General information:* Image segmentation was performed using a custom Python analysis
484 pipeline. All code and documentation can be found on GitHub
485 (https://github.com/AltschulerWu-Lab/MAGS). Starting with maximum intensity projections of
486 Hoechst, EdU, Lgr5-GFP, Muc2, Lyz, and ChgA fluorescent images, we segmented and then
487 quantified numbers of nuclei, EdU^+ cells, stem cells, goblet cells, Paneth cells, and
488 enteroendocrine cells, respectively. The general segmentation process for each object type
489 consisted of two major steps: a thresholding step to identify image foreground, and a
490 segmentation step to generate location and boundary of objects. Specific details are as follows:
491

492 *Segmenting nuclei:* Hoechst stain images were smoothed through convolution with a bilateral
493 filter. The foreground was identified using a modified Otsu threshold method. Nuclei in enteroid
494 cultures are highly heterogeneous with small, tightly packed nuclei in the crypt regions and large,
495 sparsely distributed nuclei in the villus regions. Therefore, to obtain an accurate segmentation in
496 these different regions, we conducted a two-step segmentation approach. First, sparse nuclei
497 were identified using a multi-scale Laplacian of Gaussian (LoG) detector to generate markers of
498 object locations. A watershed algorithm was then used to generate object boundaries. Clumps
499 were detected in the sparse segmentation using object size and shape irregularity cutoffs. These
500 clumps contained mis-segmented dense nuclei and were subsequently segmented using
501 differently parameterized LoG detector to identify object seeds and watershed to generate object
502 boundaries. The dense and sparse segmentations were then merged for the final result (also see
503 Figure 1-Supplement 1C).
504

505 *Segmenting EdU^+ nuclei:* The same process as nuclear segmentation was used because nuclear
506 objects in EdU stain images had similar properties as those in Hoechst stain images.
507 *Segmenting stem cells (Figure 1-Supplement 1D):* GFP immunofluorescence in enteroid
508 monolayers derived from Lgr5-eGFP-DTR mice (H. Tian et al., 2011) revealed both crypt
509 regions, with multi-cell membrane GFP staining, and single GFP^+ cells outside crypt regions.
510 The single GFP^+ cells appeared morphologically similar to tuft cells and co-stained for Dclk-1
511 (Figure 1-Supplement 1E), indicating that these cells are likely a subpopulation of tuft cells
512 rather than stem cells. Therefore, we only identified stem cells within crypt regions. Crypt

513 regions were defined as clusters of Lgr5^{+} stem and Paneth cells, corresponding to crypt bases *in*
514 *vivo*. Lgr5-GFP stain images were processed to remove tissue background and thresholded to
515 identify foreground. Holes and gaps in crypt regions were filled using morphological operations
516 and small objects (typically, Lgr5^{+}/Dclk1^{+} cells, see Figure 1-Supplement 1E) were dropped. The
517 remaining objects were labeled as crypts. We then counted nuclei within crypt regions as stem
518 cells. Importantly, we removed any nucleus in a crypt region that was associated with a Paneth
519 cell from the stem cell count (Figure 1-Supplement 1A).
520
521 *Identifying Paneth cells:* Lysozyme (Lyz) immunofluorescence images were smoothed through
522 convolution with a bilateral filter then a tophat filter. Foreground was identified using the Otsu-
523 thresholded Lyz immunofluorescence image. A LoG detector was then used to generate markers
524 of Paneth object locations.
525
526 *Segmenting goblet cells:* Mucin-2 (Muc2) stain images were smoothed by convolution with a
527 median filter. Foreground was identified using a convex hull of objects in each Otsu-thresholded
528 Muc2 immunofluorescence image. Goblet cells were segmented using a LoG detector to
529 generate markers of goblet object locations followed by watershed to create object boundaries.
530
531 *Identifying enteroendocrine (EE) cells:* ChgA stain images were processed using the same steps
532 as Paneth cell identification, only with different parameters.
533
534 *Evaluation of Image Segmentation:* Each cell-type object (e.g., each nucleus, each goblet cell,
535 each Paneth cell) was identified in raw immunofluorescence images by hand by an expert and, in
536 parallel, using the customized algorithms described above. The expert-generated segmented
537 images (where each mask represents an individual object) were compared to algorithm-generated
538 segmented images to determine algorithm performance. 'Precision' was quantified by dividing
539 the number of true positives (expert-identified objects also identified by the algorithm) by the
540 number of total positives (all algorithm-identified objects). 'Recall' was quantified by dividing
541 the number of true positives by the total number of expert-identified objects. F1 scores were
542 calculated as the harmonic mean of precision and recall. See Table 1 for results.
543

544 Data Analysis

545 *Extracting numbers of each cell-type:* Due to limitations of conventional fluorescence
546 microscopy, all desired cell-types were quantified across two replicate immunofluorescent stain
547 sets: a crypt stain set (Hoechst, EdU, Lgr5-GFP, Lyz) and a differentiated cell stain set (Hoechst,
548 EdU, Muc2, ChgA). We were able to quantify the numbers of some cell-types directly from a
549 single stain set, including the number of each directly measured cell-type (EdU^+, stem, goblet,
550 Paneth, EE) as well the number of proliferating (EdU^+) stem cells (combining information from
551 EdU and Lgr5-GFP segmentation), transit-amplifying cells (TA; #EdU^+ cells minus #stem cells),
552 and differentiated cells (# cells minus stem and TA cells).
553
554 *Replicates and Error Estimation:* In-plate replicate control wells (2-6 wells per plate) were used
555 to estimate mean and error. For replicate plates, mean and error were pooled. For across stain-set
556 readouts, error was propagated.
557
558 *Fold Change:* We calculated fold-change effects relative to in-plate controls for readouts within
559 each stain set (#EdU^+ stem cell, #TA cells). Fold-changes for readouts calculated across both
560 stain sets (#secretory/#diff, #goblet/#secretory, #Paneth/#secretory, #EE/#secretory) were
561 calculated to a pooled control baseline measurement.
562
563 Statistical testing

564 In comparing enteroid samples, two-sided Welch's t-tests were performed and p values were
565 reported. In comparing *in vivo* samples, two-sided Student's t tests were performed and p values
566 were reported. Degrees of freedom is taken as n-1. Measurements were taken from distinct
567 samples.
568
569 Perturbation effect visualization

570 For Figure 2B, double perturbation phenotypes were sorted into similar phenotypes using
571 hierarchical clustering (clustermap function in seaborn) with a euclidean distance metric. Single
572 perturbation phenotypes were sorted based on the number of EdU^+ stem cells in each row.
573
574

575 Population growth model

576 We established a simple population growth model to compute the changes in secretory and
577 absorptive populations in response to cell cycle perturbation. In this model, we assumed that the
578 initial ratio of absorptive to secretory TA progenitors produced by stem cells is equal. We further
579 assumed that the progenitors are locked into either secretory or absorptive fates after the initial
580 commitment with no switching occurring between fates (Stamataki et al., 2011; van Es et al.,
581 2012). The model describes the theoretical output of differentiated cells from populations of
582 initial secretory or absorptive progenitors.

583 Under normal growth (control condition), we describe the amplification of absorptive and
584 secretory TA cells as follows:

585 $$A = A_0(2)^{\frac{t}{\tau_a}}$$

586 $$S = S_0(2)^{\frac{t}{\tau_s}}$$

587 where A_0 and S_0 are the numbers of initial absorptive and secretory TA progenitors, respectively.
588 A and S are the numbers of final absorptive and secretory differentiated cells, respectively. t is
589 the total model time, set to be 48 (hours). τ_a and τ_s are the cell cycle lengths of absorptive and
590 secretory progenitors, respectively. Absorptive progenitors are generally found to divide 4-5
591 times while secretory progenitors only divide 1-2 times (Potten, 1998; Stamataki et al., 2011; van
592 Es et al., 2012). We set τ_a and τ_s to be 12 and 48 (hours) in control conditions. Thus, secretory
593 progenitors divide once while absorptive progenitors divide four times before fully
594 differentiating, consistent with previous observations. Progenitors that divide fewer times are not
595 considered differentiated cells.

596 We model the perturbation effect with the parameter p, where p is the probability of cell cycle
597 progression for any TA cell (alternatively 1 – p is the probability of quiescence). The expected
598 numbers of differentiated absorptive and secretory cells, as averaged over an ensemble of initial
599 progenitor populations, are as follows:

600 $$E(A) = A_0(2p)^{\frac{t}{\tau_a}}$$

601 $$E(S) = S_0(2p)^{\frac{t}{\tau_s}}$$

602 where $0 < p < 1$ in the case of cell cycle inhibitors and $p = 1$ in the untreated case.

603 Scanning through different values of τ_a and τ_s, we observe that as long as τ_a is less than τ_s,
604 decreasing proliferation (increasing p) corresponds to an increase in secretory prevalence. The
605 expectation follows from the observation that p modifies the expected number of progeny per

606 generation to be $2p$. More explicitly, the expectation of progeny number (X_i) for progenitor
607 generation i can be calculated as follows:

608 $$E(X_0) = \sum(E(X_{1j})) = 2p\big(E(X_1)\big) \ldots = (2p)^{\#divisions} = (2p)^{\frac{t}{\tau}}$$

609 We note that we can take a different parametrization for the cell-cycle inhibitor effect where the
610 length of cell cycling is varied under perturbation. The equations for this parametrization are as
611 follows:

612 $$A = A_0(2)^{\frac{t}{p'\tau_a}}$$

613 $$S = S_0(2)^{\frac{t}{p'\tau_s}}$$

614 where we take p' to be a number > 1 in the case of cell cycle inhibitors and p = 1 in the untreated
615 case and t is 48 as before. In this approach, we do not lose progenitors to quiescence and all
616 progenitors are considered differentiated at the end of the experiment time t. Since we can
617 convert between p' and p by letting $p = 2^{\frac{1}{p'}-1}$, we would observe a similar outcome as the first
618 parametrization approach where increasing perturbation effect via increased cell cycle inhibition
619 corresponds to an increase in secretory prevalence.
620
621 <u>Identifying perturbation interactions</u>
622 *Multiplicative model:* To identify perturbation interactions, we first established a model for how
623 perturbation effects should combine if there is no interaction. A simple model commonly used in
624 genetic and drug interaction studies is the multiplicative model (Mani et al., 2008; van Hasselt &
625 Iyengar, 2019). Under the multiplicative model, perturbations that do not interact should
626 combine as the product of their respective fold-change effects. This is equivalent to log-
627 additivity, which can be calculated as follows:
628 $\log_2 fc(AB_{predicted}) = \log_2 fc(A_{obs}) + \log_2 fc(B_{obs})$
629 Features with 0 values had a pseudocount of 1 instead. Perturbation combination effects that
630 deviate from the multiplicative model indicate a potential interaction, which we define
631 biologically as the due to utilization of a shared pathway or redundant pathways (Dixon et al.,
632 2009).
633 For each perturbation pair, we evaluated how a multiplicative model fits the observed double
634 perturbation effects for each cell-type readout (e.g., #TA cells). To evaluate the multiplicative
635 model across each perturbation and readout, we plotted the effects of perturbation combinations
636 (e.g, the effects of Wnt3a in combination with all other perturbations on #TA cells) against the

637 single perturbations (e.g., all perturbations except Wnt3a) in log scale. The multiplicative model
638 prediction is a line offset on the y-axis by the effect of the perturbation of interest (Figure 3-
639 Supplement 1B). Combinations of perturbations that do not exhibit an interaction will have an
640 effect that lies on this line. We compared linear and multiplicative functions for each single
641 perturbation and observed that some single perturbations fit well with either multiplicative or
642 linear fit models, while others deviated significantly from both (e.g., Wnt3a fits well with either
643 model while EGFR-i deviates significantly from both, see Figure 3-Supplement 1B-C). We
644 computed the residuals for perturbation combination fit across all readouts. The two models had
645 similar distributions of residual values with peaks close to zero (Figure 3-Supplement 1A),
646 indicating that the majority of perturbations in our experiment combined in a manner that is well
647 described by the multiplicative model.
648
649 *Effect size:* The deviation of each combinatorial perturbation from the prediction of the
650 multiplicative model is represented as effect size, which was quantified in this case as absolute
651 Cohen's d, or the standardized deviation of the combinatorial phenotype from multiplicative
652 model prediction.
653 Effect size = $| \mu_{obs} - \mu_{pred} | / \sigma_{pooled}$
654 where μ_{obs} and μ_{pred} are the observed and predicted means for the combination effect and σ_{pooled} is
655 the pooled standard deviation. In Figure 3A, the cut-off for the effect size was 5.
656
657 <u>BMP2 ELISA</u>
658 Supernatant levels of BMP2 were quantified using a BMP-2 Quantikine ELISA kit (R&D
659 Systems #DBP200), without significant deviations from manufacturer's instructions.
660
661 <u>qRT-PCR</u>
662 RNA was harvested from enteroid monolayers using an RNEasy Plus Mini Kit (Qiagen #74136).
663 Reverse transcription was performed using iScript Reverse Transcription kit (Bio-Rad
664 #1708841). Quantitative PCR was performed using SsoAdvanced Universal SYBR Green
665 Supermix (Bio-Rad #1725272) on a BioRad CFXConnect. Test gene values were normalized to
666 beta-actin values. To quantify Atoh1/Hes1 ratio, both Atoh1 and Hes1 fold-changes relative to

667 control were calculated and then Atoh1 fold-change was divided by Hes1 fold-change. RNA
668 levels were determined using the following primers:

Target mRNA	Forward Primer	Reverse Primer
Atoh1	5'-TCCCCTTCCTCCTACCTTCTCC-3'	5'-CAACACGCAAGGATGAACTCCC-3'
Hes1	5'-AGAAGAGGCGAAGGGCAAGAAT-3'	5'-TGGAATGCCGGGAGCTATCTTT-3'
Lyz	5'-AAGAATGCCTGTGGGATCAA-3'	5'-CGGTTTTGACATTGTGTTCG-3'
Muc2	5'-ACCCCAAGCCCTTCTCCTACTA-3'	5'-AGTGGATTGAGAGGTCACAGGC-3'
ChgA	5'-GCAACACAGCAGCTTTGAGGAT-3'	5'-GTTAGGCTCTGGAAAGGCCTGA-3'
Bmp2	5'-GCTTCTTAGACGGACTGCGG-3'	5'-GCAACACTAGAAGACAGCGGGT-3'
beta-actin	5'-CGCCACCAGTTCGCCATGGA-3'	5'-TACAGCCCGGGGAGCATCGT-3'

669

670 **Acknowledgments**

671 We are grateful to Zev Gartner, Ophir Klein, Curtis Thorne, and members of the Altschuler-Wu
672 lab for their feedback. We additionally thank Ophir Klein and Frederic de Sauvage for mouse
673 resources. This work was supported by NIH GM112690 (S.J.A.), NCI-NIH RO1 CA184984
674 (L.F.W.), the UCSF Program for Breakthrough Biomedical Research which is partly funded by
675 the Sandler Foundation (L.F.W.), NIH NRSA fellowship F32DK120102 (L.E.S.), and NSF
676 GRFP fellowship 1650113 (I.W.C.).

677 **Author contributions**

678 I.W.C. and L.E.S. conceptualized study, developed computational methods, designed and
679 executed experiments, analyzed data, and wrote the manuscript. J.M.B. and V.S. designed and

680 executed *in vivo* experiments and analyzed data. B.H. supervised the *in vivo* study. L.F.W. and

681 S.J.A. conceptualized and supervised the overall study and wrote the manuscript.

682 **Competing interests**

683 Authors declare no competing interests.

684 **References**

685 Balázsi, G., van Oudenaarden, A., & Collins, J. J. (2011). Cellular decision making and biological noise:
686 from microbes to mammals. *Cell*, *144*(6), 910–925.

687 Barnard, J. A., Beauchamp, R. D., Coffey, R. J., & Moses, H. L. (1989). Regulation of intestinal epithelial
688 cell growth by transforming growth factor type beta. In *Proceedings of the National Academy of*
689 *Sciences* (Vol. 86, Issue 5, pp. 1578–1582). https://doi.org/10.1073/pnas.86.5.1578

690 Basak, O., Beumer, J., Wiebrands, K., Seno, H., van Oudenaarden, A., & Clevers, H. (2017a). Induced
691 Quiescence of Lgr5+ Stem Cells in Intestinal Organoids Enables Differentiation of Hormone-
692 Producing Enteroendocrine Cells. *Cell Stem Cell*, *20*(2), 177–190.e4.

693 Batlle, E., Henderson, J. T., Beghtel, H., van den Born, M. M. W., Sancho, E., Huls, G., Meeldijk, J.,
694 Robertson, J., van de Wetering, M., Pawson, T., & Clevers, H. (2002). Beta-catenin and TCF
695 mediate cell positioning in the intestinal epithelium by controlling the expression of EphB/ephrinB.
696 *Cell*, *111*(2), 251–263.

697 Beumer, J., & Clevers, H. (2016). Regulation and plasticity of intestinal stem cells during homeostasis
698 and regeneration. *Development* , *143*(20), 3639–3649.

699 Birchenough, G. M. H., Nyström, E. E. L., Johansson, M. E. V., & Hansson, G. C. (2016). A sentinel
700 goblet cell guards the colonic crypt by triggering Nlrp6-dependent Muc2 secretion. *Science*,
701 *352*(6293), 1535–1542.

702 Bjerknes, M., & Cheng, H. (1999). Clonal analysis of mouse intestinal epithelial progenitors.
703 *Gastroenterology*, *116*(1), 7–14.

704 Cheng, H., & Leblond, C. P. (1974a). Origin, differentiation and renewal of the four main epithelial cell
705 types in the mouse small intestine. I. Columnar cell. *The American Journal of Anatomy*, *141*(4),
706 461–479.

707 Cheng, H., & Leblond, C. P. (1974b). Origin, differentiation and renewal of the four main epithelial cell
708 types in the mouse small intestine. V. Unitarian Theory of the origin of the four epithelial cell types.

709 *The American Journal of Anatomy*, *141*(4), 537–561.

710 Clevers, H. (2013). The intestinal crypt, a prototype stem cell compartment. *Cell*, *154*(2), 274–284.

711 Coster, A. D., Thorne, C. A., Wu, L. F., & Altschuler, S. J. (2017). Examining Crosstalk among
712 Transforming Growth Factor β, Bone Morphogenetic Protein, and Wnt Pathways. *The Journal of*
713 *Biological Chemistry*, *292*(1), 244–250.

714 Dames, P., Bergann, T., Fromm, A., Bücker, R., Barmeyer, C., Krug, S. M., Fromm, M., & Schulzke, J.-
715 D. (2015). Interleukin-13 affects the epithelial sodium channel in the intestine by coordinated
716 modulation of STAT6 and p38 MAPK activity. *The Journal of Physiology*, *593*(24), 5269–5282.

717 Dixon, S. J., Costanzo, M., Baryshnikova, A., Andrews, B., & Boone, C. (2009). Systematic mapping of
718 genetic interaction networks. *Annual Review of Genetics*, *43*, 601–625.

719 Farin, H. F., Jordens, I., Mosa, M. H., Basak, O., Korving, J., Tauriello, D. V. F., de Punder, K., Angers,
720 S., Peters, P. J., Maurice, M. M., & Clevers, H. (2016). Visualization of a short-range Wnt gradient
721 in the intestinal stem-cell niche. *Nature*, *530*(7590), 340–343.

722 Flentjar, N., Chu, P.-Y., Ng, A. Y.-N., Johnstone, C. N., Heath, J. K., Ernst, M., Hertzog, P. J., &
723 Pritchard, M. A. (2007). TGF-betaRII rescues development of small intestinal epithelial cells in
724 Elf3-deficient mice. *Gastroenterology*, *132*(4), 1410–1419.

725 Flier, L. G. van der, van der Flier, L. G., & Clevers, H. (2009). Stem Cells, Self-Renewal, and
726 Differentiation in the Intestinal Epithelium. In *Annual Review of Physiology* (Vol. 71, Issue 1, pp.
727 241–260). https://doi.org/10.1146/annurev.physiol.010908.163145

728 Goldman, D. C., Donley, N., & Christian, J. L. (2009). Genetic interaction between Bmp2 and Bmp4
729 reveals shared functions during multiple aspects of mouse organogenesis. *Mechanisms of*
730 *Development*, *126*(3-4), 117–127.

731 Haber, A. L., Biton, M., Rogel, N., Herbst, R. H., Shekhar, K., Smillie, C., Burgin, G., Delorey, T. M.,
732 Howitt, M. R., Katz, Y., Tirosh, I., Beyaz, S., Dionne, D., Zhang, M., Raychowdhury, R., Garrett,
733 W. S., Rozenblatt-Rosen, O., Shi, H. N., Yilmaz, O., … Regev, A. (2017). A single-cell survey of
734 the small intestinal epithelium. *Nature*, *551*(7680), 333–339.

735 Han, L., Diehl, A., Nguyen, N. K., Korangath, P., Teo, W., Cho, S., Kominsky, S., Huso, D. L.,
736 Feigenbaum, L., Rein, A., Argani, P., Landberg, G., Gessler, M., & Sukumar, S. (2014). The Notch
737 pathway inhibits TGFβ signaling in breast cancer through HEYL-mediated crosstalk. *Cancer*
738 *Research*, *74*(22), 6509–6518.
739 Hong, S. P., Song, S., Cho, S. W., Lee, S., Koh, B. I., Bae, H., Kim, K. H., Park, J.-S., Do, H.-S., Im, I.,
740 Heo, H. J., Ko, T. H., Park, J.-H., Youm, J. B., Kim, S.-J., Kim, I., Han, J., Han, Y.-M., & Koh, G.
741 Y. (2017). Generation of PDGFRα Cardioblasts from Pluripotent Stem Cells. *Scientific Reports*, *7*,
742 41840.
743 Houde, M., Laprise, P., Jean, D., Blais, M., Asselin, C., & Rivard, N. (2001). Intestinal epithelial cell
744 differentiation involves activation of p38 mitogen-activated protein kinase that regulates the
745 homeobox transcription factor CDX2. *The Journal of Biological Chemistry*, *276*(24), 21885–21894.
746 Lander, A. D., Gokoffski, K. K., Wan, F. Y. M., Nie, Q., & Calof, A. L. (2009). Cell lineages and the
747 logic of proliferative control. *PLoS Biology*, *7*(1), e15.
748 Li, Y., Liu, Y., Liu, B., Wang, J., Wei, S., Qi, Z., Wang, S., Fu, W., & Chen, Y.-G. (2018). A growth
749 factor-free culture system underscores the coordination between Wnt and BMP signaling in Lgr5
750 intestinal stem cell maintenance. *Cell Discovery*, *4*, 49.
751 Mani, R., St Onge, R. P., Hartman, J. L., 4th, Giaever, G., & Roth, F. P. (2008). Defining genetic
752 interaction. *Proceedings of the National Academy of Sciences of the United States of America*,
753 *105*(9), 3461–3466.
754 Matsu-Ura, T., Dovzhenok, A., Aihara, E., Rood, J., Le, H., Ren, Y., Rosselot, A. E., Zhang, T., Lee, C.,
755 Obrietan, K., Montrose, M. H., Lim, S., Moore, S. R., & Hong, C. I. (2016). Intercellular Coupling
756 of the Cell Cycle and Circadian Clock in Adult Stem Cell Culture. *Molecular Cell*, *64*(5), 900–912.
757 Papin, J. A., Hunter, T., Palsson, B. O., & Subramaniam, S. (2005). Reconstruction of cellular signalling
758 networks and analysis of their properties. *Nature Reviews. Molecular Cell Biology*, *6*(2), 99–111.
759 Potten, C. S. (1998). Stem cells in gastrointestinal epithelium: numbers, characteristics and death.
760 *Philosophical Transactions of the Royal Society of London. Series B, Biological Sciences*,

761 *353*(1370), 821–830.

762 Qi, Z., Li, Y., Zhao, B., Xu, C., Liu, Y., Li, H., Zhang, B., Wang, X., Yang, X., Xie, W., Li, B., Han, J.-
763 D. J., & Chen, Y.-G. (2017). BMP restricts stemness of intestinal Lgr5 stem cells by directly
764 suppressing their signature genes. *Nature Communications*, *8*, 13824.

765 Ramirez, M., Rajaram, S., Steininger, R. J., Osipchuk, D., Roth, M. A., Morinishi, L. S., Evans, L., Ji, W.,
766 Hsu, C.-H., Thurley, K., Wei, S., Zhou, A., Koduru, P. R., Posner, B. A., Wu, L. F., & Altschuler, S.
767 J. (2016). Diverse drug-resistance mechanisms can emerge from drug-tolerant cancer persister cells.
768 *Nature Communications*, *7*, 10690.

769 Richmond, C. A., Rickner, H., Shah, M. S., Ediger, T., Deary, L., Zhou, F., Tovaglieri, A., Carlone, D. L.,
770 & Breault, D. T. (2018a). JAK/STAT-1 Signaling Is Required for Reserve Intestinal Stem Cell
771 Activation during Intestinal Regeneration Following Acute Inflammation. *Stem Cell Reports*, *10*(1),
772 17–26.

773 Rodríguez-Colman, M. J., Schewe, M., Meerlo, M., Stigter, E., Gerrits, J., Pras-Raves, M., Sacchetti, A.,
774 Hornsveld, M., Oost, K. C., Snippert, H. J., Verhoeven-Duif, N., Fodde, R., & Burgering, B. M. T.
775 (2017). Interplay between metabolic identities in the intestinal crypt supports stem cell function.
776 *Nature*, *543*(7645), 424–427.

777 Salic, A., & Mitchison, T. J. (2008). A chemical method for fast and sensitive detection of DNA synthesis
778 in vivo. *Proceedings of the National Academy of Sciences*, *105*(7), 2415–2420.

779 Sato, T., Stange, D. E., Ferrante, M., Vries, R. G. J., Van Es, J. H., Van den Brink, S., Van Houdt, W. J.,
780 Pronk, A., Van Gorp, J., Siersema, P. D., & Clevers, H. (2011). Long-term expansion of epithelial
781 organoids from human colon, adenoma, adenocarcinoma, and Barrett's epithelium.
782 *Gastroenterology*, *141*(5), 1762–1772.

783 Sato, T., Vries, R. G., Snippert, H. J., van de Wetering, M., Barker, N., Stange, D. E., van Es, J. H., Abo,
784 A., Kujala, P., Peters, P. J., & Clevers, H. (2009). Single Lgr5 stem cells build crypt-villus structures
785 in vitro without a mesenchymal niche. *Nature*, *459*(7244), 262–265.

786 Stamataki, D., Holder, M., Hodgetts, C., Jeffery, R., Nye, E., Spencer-Dene, B., Winton, D. J., & Lewis,

787 J. (2011). Delta1 expression, cell cycle exit, and commitment to a specific secretory fate coincide
788 within a few hours in the mouse intestinal stem cell system. *PloS One*, *6*(9), e24484.
789 Thorne, C. A., Chen, I. W., Sanman, L. E., Cobb, M. H., Wu, L. F., & Altschuler, S. J. (2018). Enteroid
790 Monolayers Reveal an Autonomous WNT and BMP Circuit Controlling Intestinal Epithelial Growth
791 and Organization. *Developmental Cell*, *44*(5), 624–633.e4.
792 Tian, A., Benchabane, H., Wang, Z., & Ahmed, Y. (2016). Regulation of Stem Cell Proliferation and Cell
793 Fate Specification by Wingless/Wnt Signaling Gradients Enriched at Adult Intestinal Compartment
794 Boundaries. *PLoS Genetics*, *12*(2), e1005822.
795 Tian, H., Biehs, B., Warming, S., Leong, K. G., Rangell, L., Klein, O. D., & de Sauvage, F. J. (2011). A
796 reserve stem cell population in small intestine renders Lgr5-positive cells dispensable. *Nature*,
797 *478*(7368), 255–259.
798 van der Flier, L. G., & Clevers, H. (2009). Stem cells, self-renewal, and differentiation in the intestinal
799 epithelium. *Annual Review of Physiology*, *71*, 241–260.
800 van der Flier, L. G., Haegebarth, A., Stange, D. E., van de Wetering, M., & Clevers, H. (2009). OLFM4 is
801 a robust marker for stem cells in human intestine and marks a subset of colorectal cancer cells.
802 *Gastroenterology*, *137*(1), 15–17.
803 VanDussen, K. L., Carulli, A. J., Keeley, T. M., Patel, S. R., Puthoff, B. J., Magness, S. T., Tran, I. T.,
804 Maillard, I., Siebel, C., Kolterud, Å., Grosse, A. S., Gumucio, D. L., Ernst, S. A., Tsai, Y.-H.,
805 Dempsey, P. J., & Samuelson, L. C. (2012). Notch signaling modulates proliferation and
806 differentiation of intestinal crypt base columnar stem cells. *Development* , *139*(3), 488–497.
807 van Es, J. H., Jay, P., Gregorieff, A., van Gijn, M. E., Jonkheer, S., Hatzis, P., Thiele, A., van den Born,
808 M., Begthel, H., Brabletz, T., Taketo, M. M., & Clevers, H. (2005). Wnt signalling induces
809 maturation of Paneth cells in intestinal crypts. *Nature Cell Biology*, *7*(4), 381–386.
810 van Es, J. H., Sato, T., van de Wetering, M., Lyubimova, A., Nee, A. N. Y., Gregorieff, A., Sasaki, N.,
811 Zeinstra, L., van den Born, M., Korving, J., Martens, A. C. M., Barker, N., van Oudenaarden, A., &
812 Clevers, H. (2012). Dll1+ secretory progenitor cells revert to stem cells upon crypt damage. *Nature*

813 *Cell Biology*, *14*(10), 1099–1104.

814 van Hasselt, J. G. C., & Iyengar, R. (2019). Systems Pharmacology: Defining the Interactions of Drug
815 Combinations. *Annual Review of Pharmacology and Toxicology*, *59*, 21–40.

816 von Moltke, J., Ji, M., Liang, H.-E., & Locksley, R. M. (2015). Tuft-cell-derived IL-25 regulates an
817 intestinal ILC2–epithelial response circuit. *Nature*, *529*(7585), 221–225.

818 Yin, X., Farin, H. F., van Es, J. H., Clevers, H., Langer, R., & Karp, J. M. (2014a). Niche-independent
819 high-purity cultures of Lgr5+ intestinal stem cells and their progeny. *Nature Methods*, *11*(1), 106–
820 112.

821 **Figures**

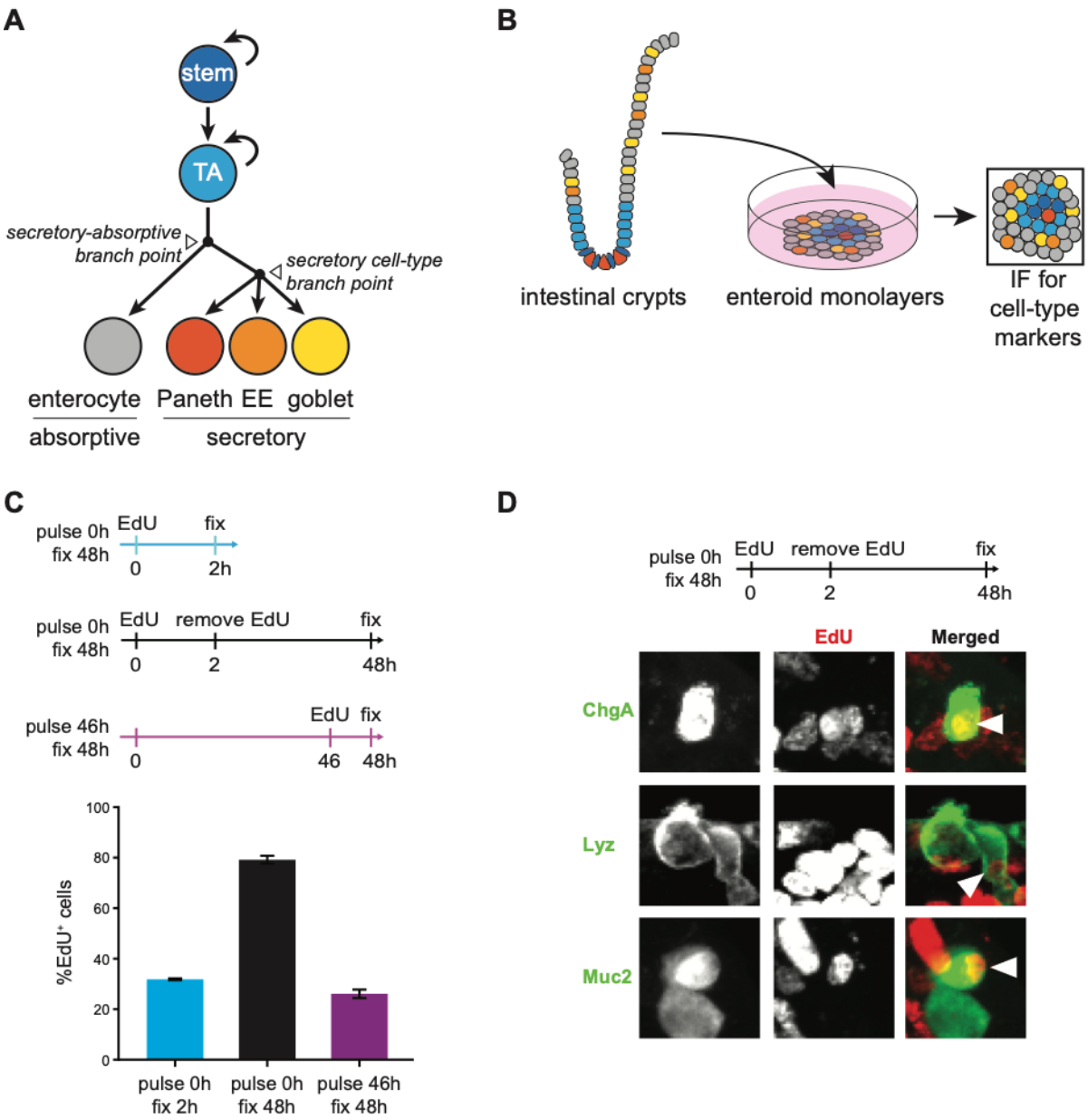

822

823 **Figure 1. A quantitative microscopy platform to study regulation of intestinal cell-type**

824 **composition.** (**A**) Intestinal epithelial cell lineage diagram. (**B**) Workflow for characterization of

825 perturbation effects on cell-type composition. Intestinal crypts are cultured as enteroid

826 monolayers. Cell-type numbers are measured from immunofluorescence (IF) images of enteroid

827 monolayers. (**C**) ~80% of cells in 48 hours of enteroid culture are produced by initial

828 progenitors. Enteroid monolayers were seeded and either EdU was added for 2 hours and
829 enteroids were then fixed (cyan), EdU was pulsed for 2 hours and removed for 46 hours before
830 fixation (black), or enteroids were cultured for 46 hours and EdU added for the 2 hours prior to
831 fixation (magenta). ~20-30% of cells are proliferating (EdU^+) upon initial seeding (cyan) and
832 after 48 hours of culture (magenta), and ~80% of cells are produced by initially proliferating
833 progenitors (EdU^+) in the 48-hour culture period (black). n=3 wells. (**D**) Initial progenitors
834 produce secretory cell-types during 48 hours of culture. Enteroids were pulsed with EdU for 2
835 hours upon initial seeding. EdU was removed and cells were fixed after 46 hours of culture. EdU
836 and cell-type marker (Lyz; Paneth, Muc2; goblet, and ChgA; EE) staining patterns were then
837 visualized. Arrowheads indicate cells that co-stain for EdU and the indicated cell-type markers.
838 Error bars mean +/- sem.

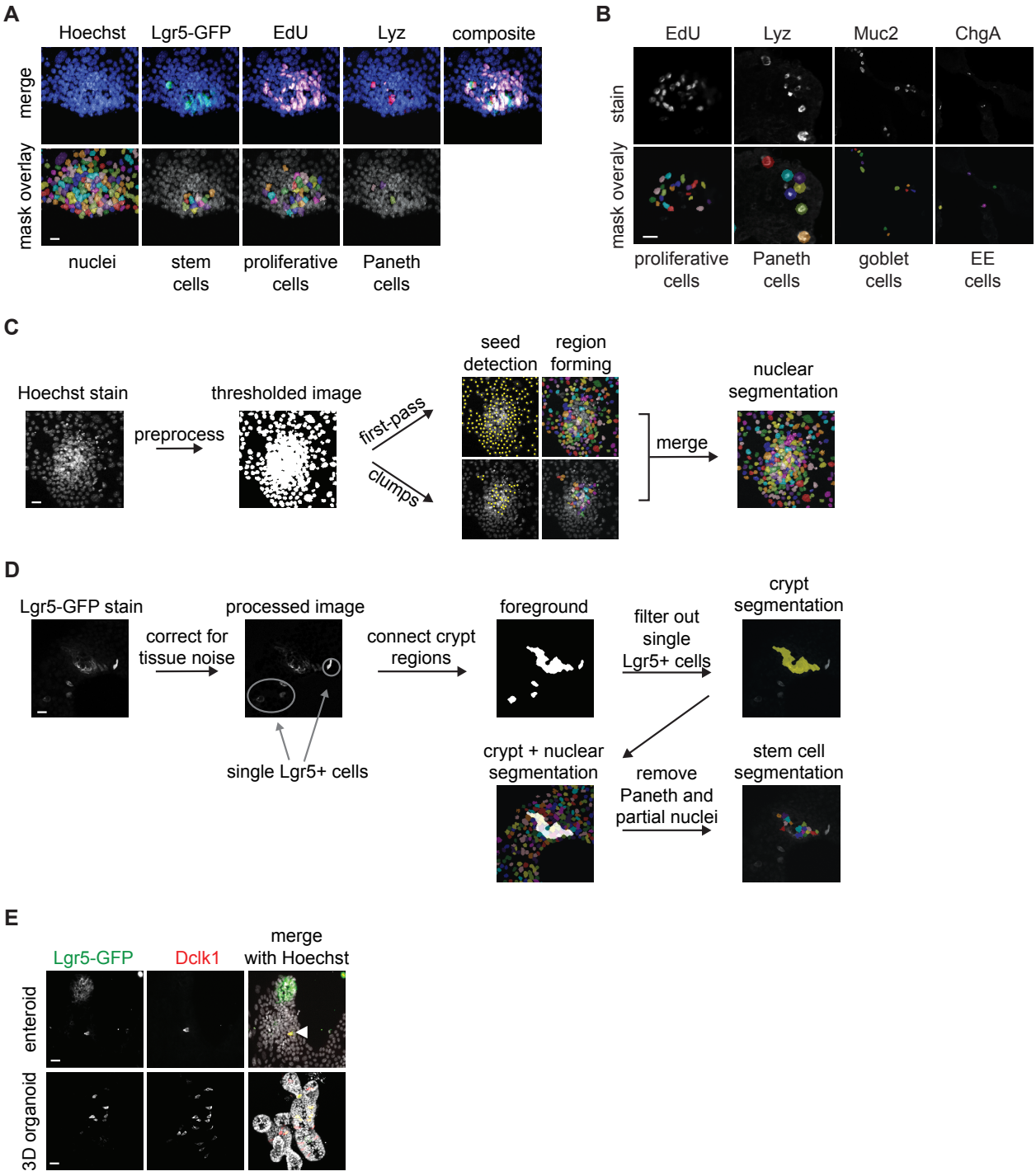

Figure 1-Supplement 1. Quantification of intestinal epithelial cell-types in immunofluorescence images of enteroid monolayers. (**A**) Example of crypt segmentation with pseudocolor overlay for each cell-type readout. Scale bar 10µm. (**B**) Example of segmentation of proliferating, Paneth, goblet, and enteroendocrine (EE) cells. Top is raw immunofluorescence

844 image for indicated marker and bottom includes pseudocolor overlay of each identified cell
845 object. Scale bar 10μm. (**C**) Schematic of nuclear segmentation steps. Thresholded Hoechst stain
846 images were segmented in two passes. The first pass segmented sparse nuclei and the second
847 pass segmented clumped nuclei. Sparse and clumped segmentation were merged into the final
848 nuclear segmentation. Yellow dots indicate identified markers of nuclear object locations, multi-
849 pseudocolor overlay depicts individual nuclei segmented using a watershed algorithm. Scale bar
850 10μm. (**D**) Schematic of stem cell segmentation. The Lgr5-GFP stain was first corrected for
851 tissue noise and then thresholded. Size filtering was used to separate multi-cell membrane GFP
852 regions (crypt regions) from single Lgr5-GFP+ cells. All nuclei in crypt regions (nuclei
853 identified from Hoechst image segmentation of same region), with the exception of Paneth cell-
854 associated nuclei, were counted as stem cells. Scale bar 10μm. (**E**) Single Lgr5-GFP+ cells are
855 also Dclk1+ in enteroid monolayers (top; scale bar 10μm) and 3D organoids (bottom; scale bar
856 15μm) and are thus excluded from stem cell counts.

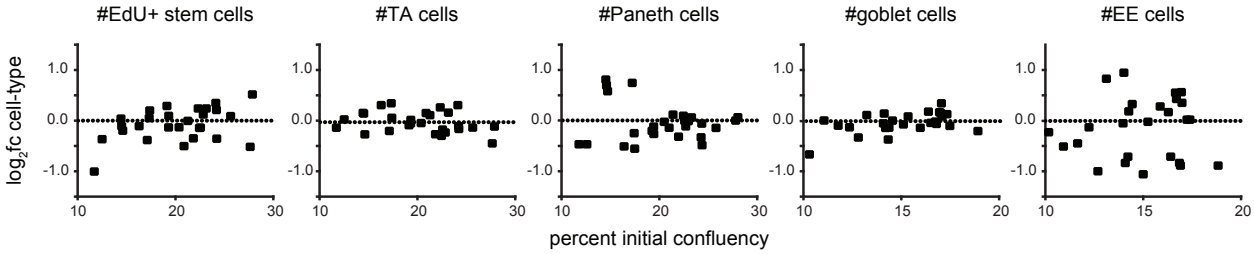

857

858 **Figure 1-Supplement 2. Enteroid monolayers exhibit reproducible cell-type composition**

859 **across replicate wells when crypts are seeded at 10-30% initial confluency.** Percent initial

860 confluency was measured from brightfield images taken after crypt seeding and 48hr cell-type

861 composition was quantified from immunofluorescence images. Y axis log_2fc was computed

862 relative to the average of all wells. No relationship is observed between initial confluency and

863 cell frequencies.

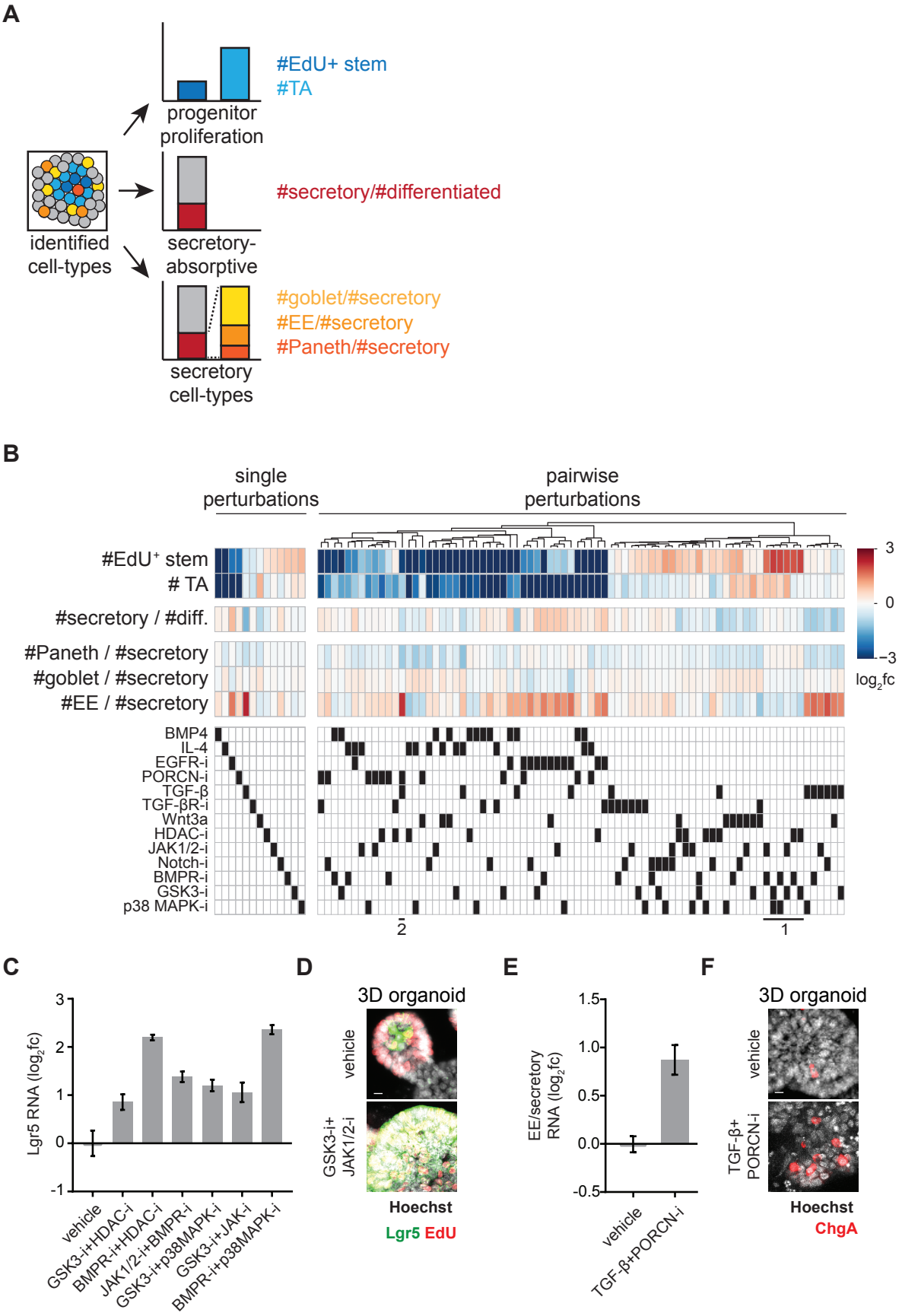
A
#EdU+ stem
#TA
progenitor proliferation
#secretory/#differentiated
identified cell-types
secretory-absorptive
#goblet/#secretory
#EE/#secretory
#Paneth/#secretory
secretory cell-types
B
single perturbations
pairwise perturbations
#EdU+ stem
TA
#secretory / #diff.
#Paneth / #secretory
#goblet / #secretory
#EE / #secretory
BMP4
IL-4
EGFR-i
PORCN-i
TGF-β
TGF-βR-i
Wnt3a
HDAC-i
JAK1/2-i
Notch-i
BMPR-i
GSK3-i
p38 MAPK-i
2
1
3
0
-3
log2fc
C
Lgr5 RNA (log2fc)
vehicle
GSK3-i+HDAC-i
BMPR-i+HDAC-i
JAK1/2-i+BMPR-i
GSK3-i+p38MAPK-i
GSK3-i+JAK-i
BMPR-i+p38MAPK-i
D
3D organoid
vehicle
GSK3-i+ JAK1/2-i
Hoechst
Lgr5 EdU
E
EE/secretory RNA (log2fc)
vehicle
TGF-β+PORCN-i
F
3D organoid
vehicle
TGF-β+ PORCN-i
Hoechst
ChgA

865 **Figure 2. Systematic characterization of perturbation effects on intestinal epithelial cell-**
866 **type composition reveals cell-type-specific regulators.** (**A**), Cell-type counts are combined to
867 quantify progenitor proliferation (top), overall secretory cell prevalence (middle), and
868 representation of each secretory cell-type within that lineage (bottom). (**B**) Combinatorial
869 perturbations induce diverse phenotypes. Single (left) and pairwise (right) perturbation effects
870 are shown. Top colored heatmaps: Perturbation effects are represented as $\log_2$ fold-change (fc)
871 relative to vehicle-treated wells. Bottom black-and-white heatmap: Black boxes indicate
872 perturbations in each column. Single perturbations are sorted by #EdU$^+$ stem cells; combinatorial
873 perturbations are clustered based on similarity of tissue-wide effects. Callouts (1) and (2)
874 referred to in text. n=2-28 wells. (**C-D**) Recapitulation of Lgr5$^+$ stem cell-inducing conditions by
875 qRT-PCR in enteroid monolayers and IF in 3D organoids. (**C**) Enteroid monolayers were treated
876 as indicated for 48 hours. RNA levels were measured by qRT-PCR. n=3 wells. (**D**) Lgr5-GFP-
877 DTR 3D organoids were treated as indicated for 48 hours. EdU was added for 2 hours prior to
878 fixation. (**E-F**) Recapitulation of EE cell inducing condition by qRT-PCR in enteroid monolayers
879 and IF in 3D organoids. (**E**) Enteroid monolayers were treated as indicated for 48 hours. Changes
880 in EE cell RNA (ChgA) relative to average of secretory cell RNA (ChgA+Lyz+Muc2) was
881 measured by qRT-PCR. n=3 wells. (**F**) 3D organoids were treated as indicated for 24 hours and
882 increased EE (ChgA$^+$) cell numbers were observed. Error bars mean +/- sem.

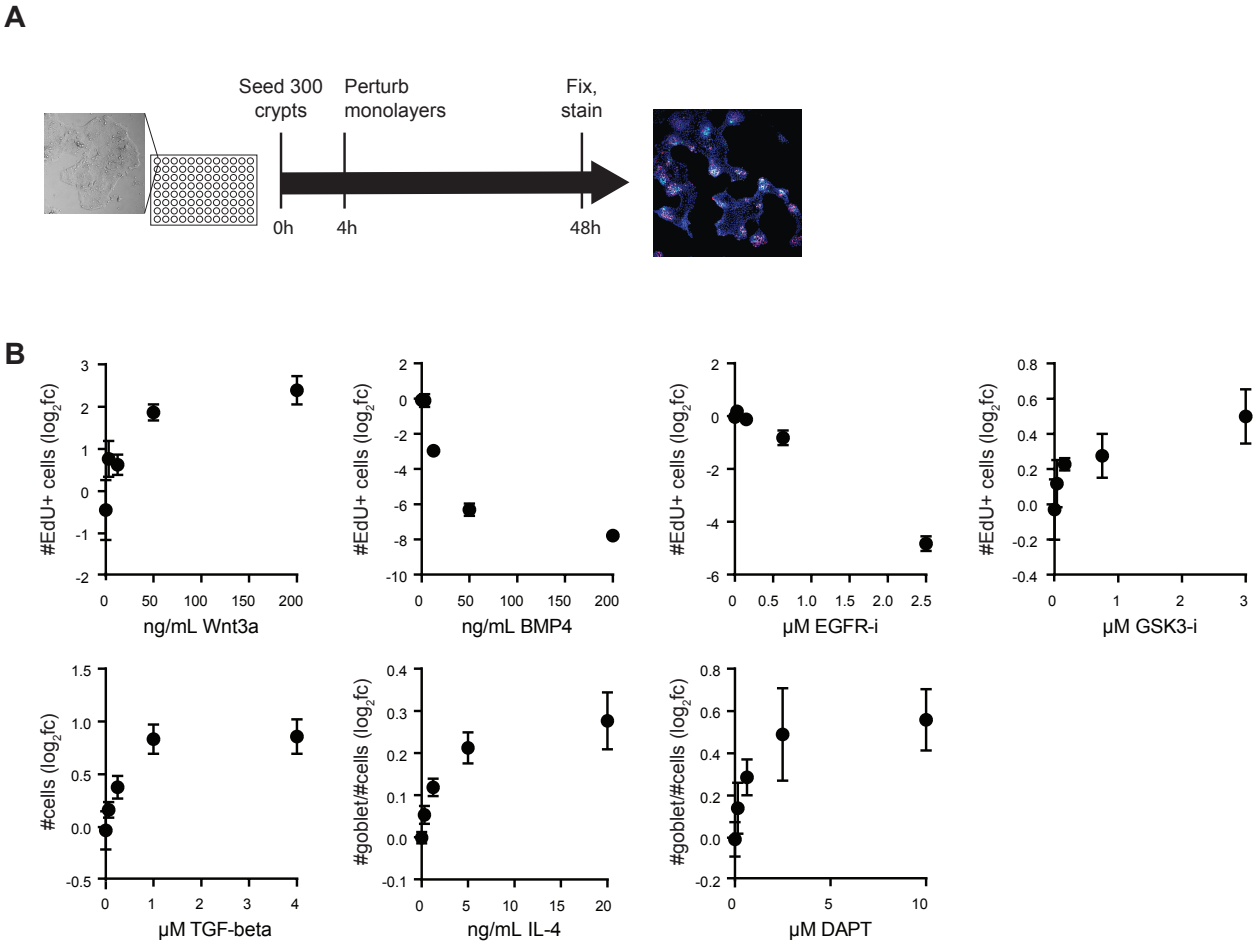

Figure 2-Supplement 1. Optimization of perturbation dose. (**A**) Schematic of experimental procedure for investigating tissue responses to perturbation. (**B**) Quantification of cell numbers and prevalence after perturbation with increasing doses of Wnt3a, BMP4, EGFR inhibitor, GSK3 inhibitor, TGF-beta, IL-4, or Notch inhibitor. All data are represented as $\log_2$ transform of the fold-change effect relative to control. Fraction of goblet cells was calculated as a percentage of all cells for comparison with previous studies. n=2-6 wells. Error bars mean +/- sem.

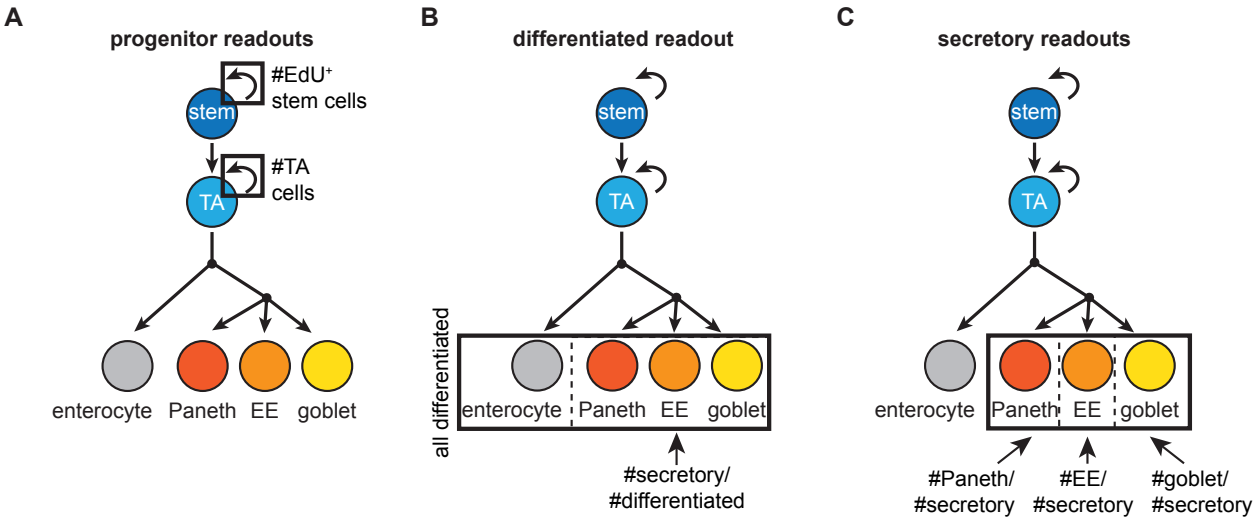

Figure 2-Supplement 2. Combining cell-type numbers into readouts of progenitor proliferation and differentiated cell composition. (**A**) Numbers of proliferating progenitors were quantified as the #EdU^{+} cells, which was further divided into proliferating stem and transit-amplifying (TA) cells based on Lgr5 staining. (**B**) The secretory-absorptive bias was quantified as the fraction of differentiated cells (EdU^{-} and Lgr5^{-}) that express secretory markers (the total number of cells that express Paneth (Lyz), goblet (Muc2), or enteroendocrine (EE) cell (ChgA) markers). (**C**) Composition of the secretory lineage was quantified as the fraction of secretory cells that express either goblet, Paneth, or EE cell markers.

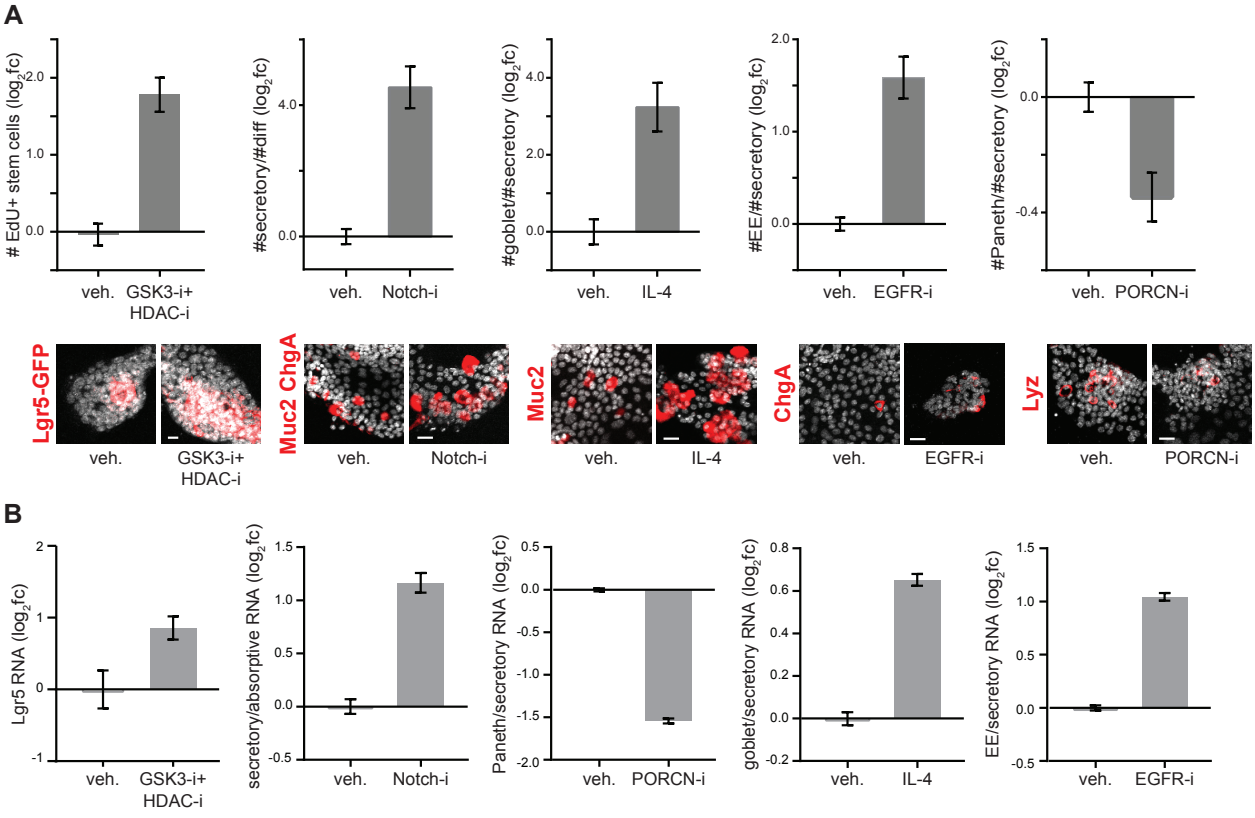

Figure 2-Supplement 3. Benchmarking enteroid monolayer responses to well-characterized perturbations. (**A**) Enteroid monolayers respond as expected to modulators of stemness (GSK3-i+HDAC-i) and secretory cell prevalence (Notch-i, IL-4, EGFR-i, PORCN-i). Both quantification of replicate wells (top, n=2-6 wells) and representative images (bottom) are shown. Scale bars 10µm. (**B**) Similar changes in cell-type composition are observed at the RNA level. Enteroid monolayers were treated as indicated for 48 hours. For secretory:absorptive RNA, the Atoh1/Hes1 ratio was measured. Paneth RNA=Lyz, goblet RNA=Muc2, EE RNA=ChgA, secretory RNA=Lyz+Muc2+ChgA. n=3 wells. Error bars mean +/- sem. Veh=vehicle.

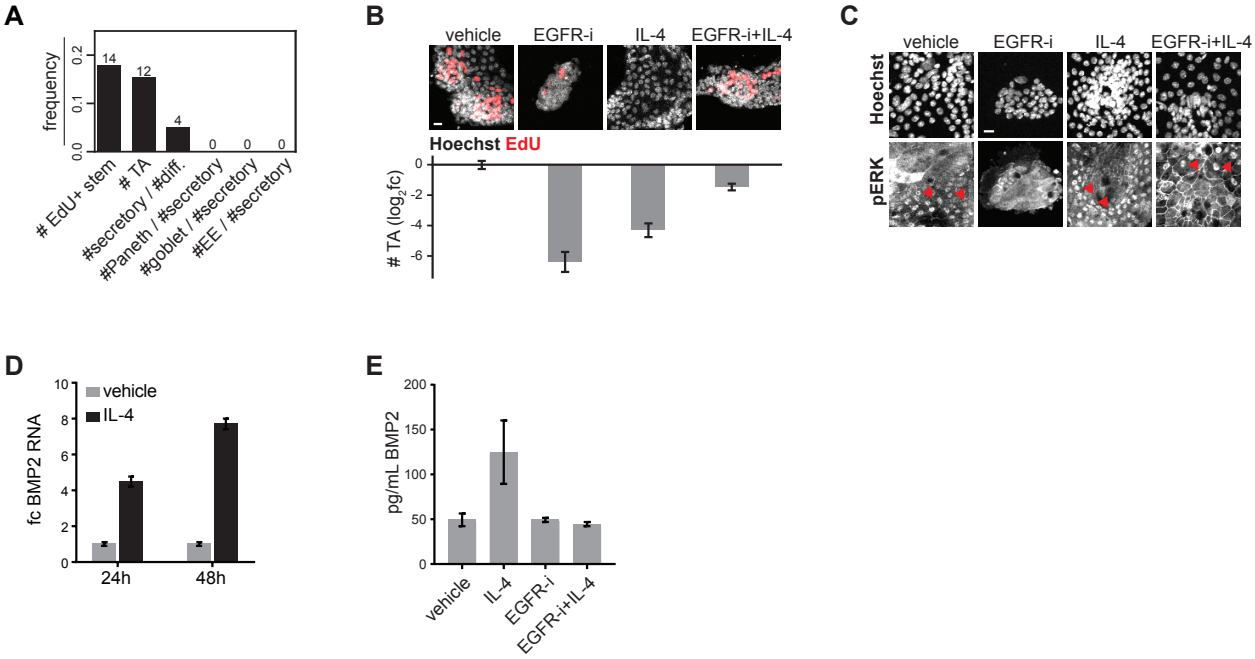

Figure 3. Interaction mapping reveals mutual antagonism between EGFR-i and IL-4. (**A**) Perturbation interactions are predominantly observed in the regulation of EdU^+ stem and TA cell numbers. The frequency of perturbation pairs that exhibit significant deviation from the multiplicative expectation was quantified for each readout of cell-type composition. (**B**) EGFR-i and IL-4 antagonize each other's effects on TA numbers. Enteroid monolayers were treated as indicated for 48 hours. Images (top) and quantification of TA cell numbers (bottom) are shown. n=2-6 wells. (**C**) IL-4 induces phospho-Erk nuclear translocation in the context of EGFR inhibition. Enteroid monolayers were treated as indicated for 48 hours and then stained for phospho-Erk. Nuclear phospho-Erk is observed in all conditions except EGFR-i alone. Red arrowheads indicate example cells with nuclear phospho-Erk. (**D**) IL-4 induces BMP2 production. Enteroid monolayers were treated as indicated and BMP2 RNA levels measured by qRT-PCR. n=3 wells. (**E**) EGFR-i abrogates the IL-4-induced increase in BMP2 production. Enteroid monolayers were treated as indicated for 48 hours and levels of BMP2 in the media measured by ELISA. n=3 wells. Error bars mean +/- sem. Fc=fold-change.

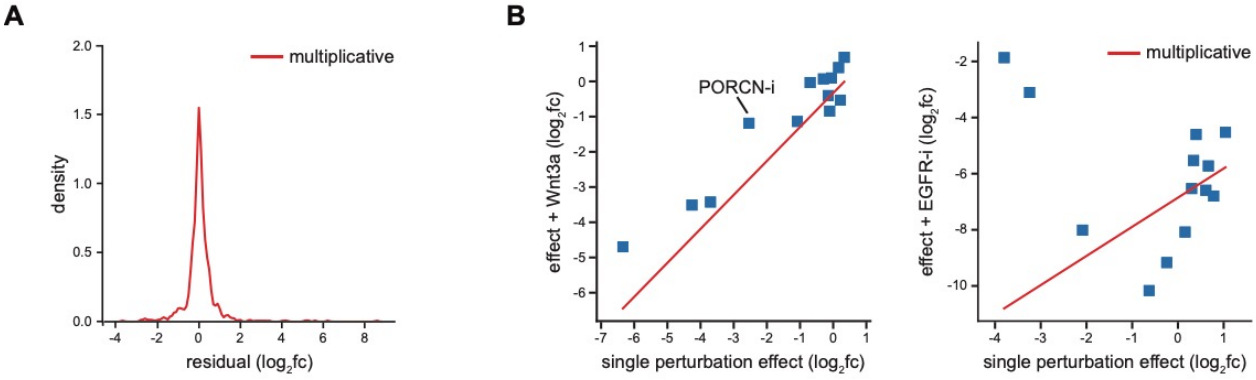

Figure 3-Supplement 1. Evaluation of the multiplicative model. (**A**) Perturbation effects are generally similar to the predictions of the multiplicative model. Distribution of residual between predicted and observed values across all cell-type readouts is shown. (**B**) Individual perturbations are either predicted by the multiplicative model or diverge significantly. Examples of well-predicted (Wnt3a) and divergent (EGFR-i) perturbations are shown. Effects shown are on #TA cells. The multiplicative model predicts an interaction between an inhibitor of PORCN, an enzyme required to process epithelial-intrinsic Wnt3a, and Wnt3a treatment (left).

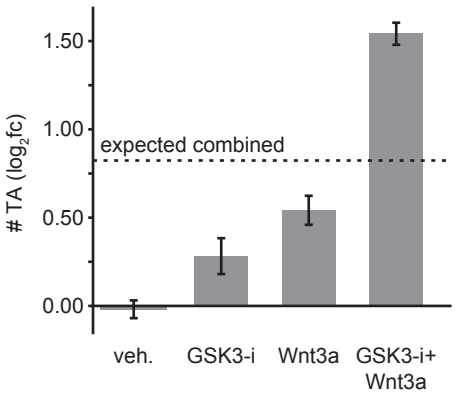

931

932 **Figure 3-Supplement 2. Example of perturbation interaction between Wnt3a and GSK3-i.**

933 The combination effect of Wnt3a and GSK3-i is much higher than would be expected under the

934 multiplicative model. This synergism can be explained by the mechanisms of Wnt3a and GSK3-i

935 as both perturbations impact components of the Wnt pathway.

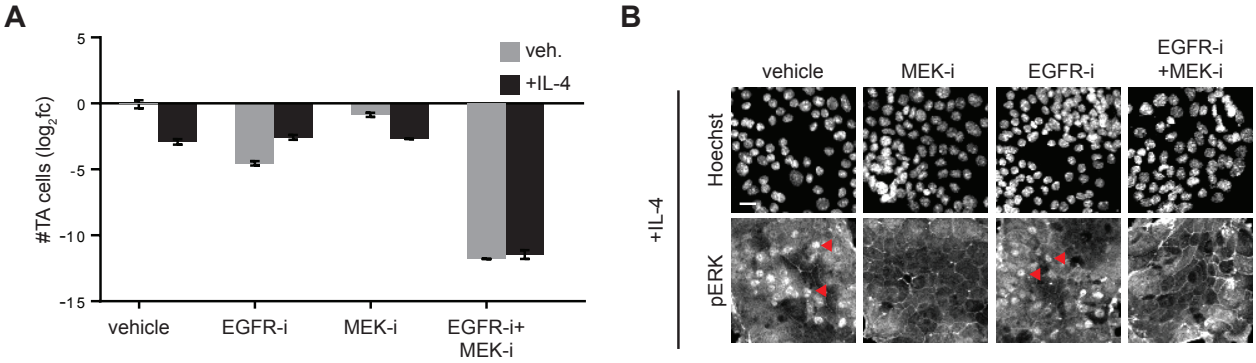

936

937 **Figure 3-Supplement 3. Regulation of MEK-Erk activity by EGFR and IL-4.** (**A**)

938 Antagonistic effect of IL-4 on EGFR-i is dependent on MEK activity. Enteroid monolayers were

939 treated as indicated for 48 hours and the number of TA cells quantified. n=2-6 wells. (**B**) MEK

940 inhibition reduces Erk activation (nuclear translocation of phospho-Erk) in enteroid monolayers

941 even in the context of IL-4 treatment. Enteroid monolayers were treated with the indicated

942 compounds for 24hr and then stained for phospho-Erk1/2. Red arrowheads indicate example

943 cells with nuclear phospho-Erk. Scale bar 7.5µm.

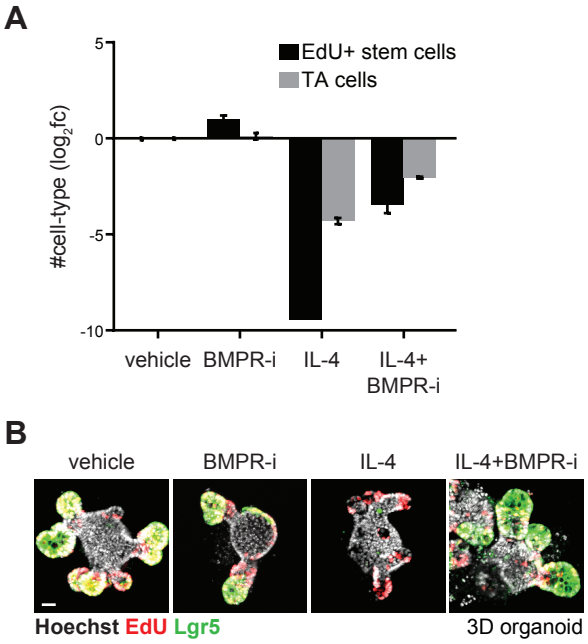

Figure 3-Supplement 4. Regulation of BMP signaling by IL-4. (**A**) BMP receptor inhibition blocks IL-4-induced downregulation of TA cell numbers and stem cell numbers. Enteroid monolayers were treated as indicated for 48 hours and both EdU^+ stem and TA cell numbers quantified. n=2-6 wells. (**B**) BMP receptor inhibition blocks IL-4-induced downregulation of proliferation and stemness in 3D organoids. 3D organoids were treated with vehicle or IL-4 in the presence and absence of BMP receptor inhibitor for 48hrs and then stained for proliferating cells (EdU^+) and stem cells ($Lgr5^+$). Scale bar 20µm.

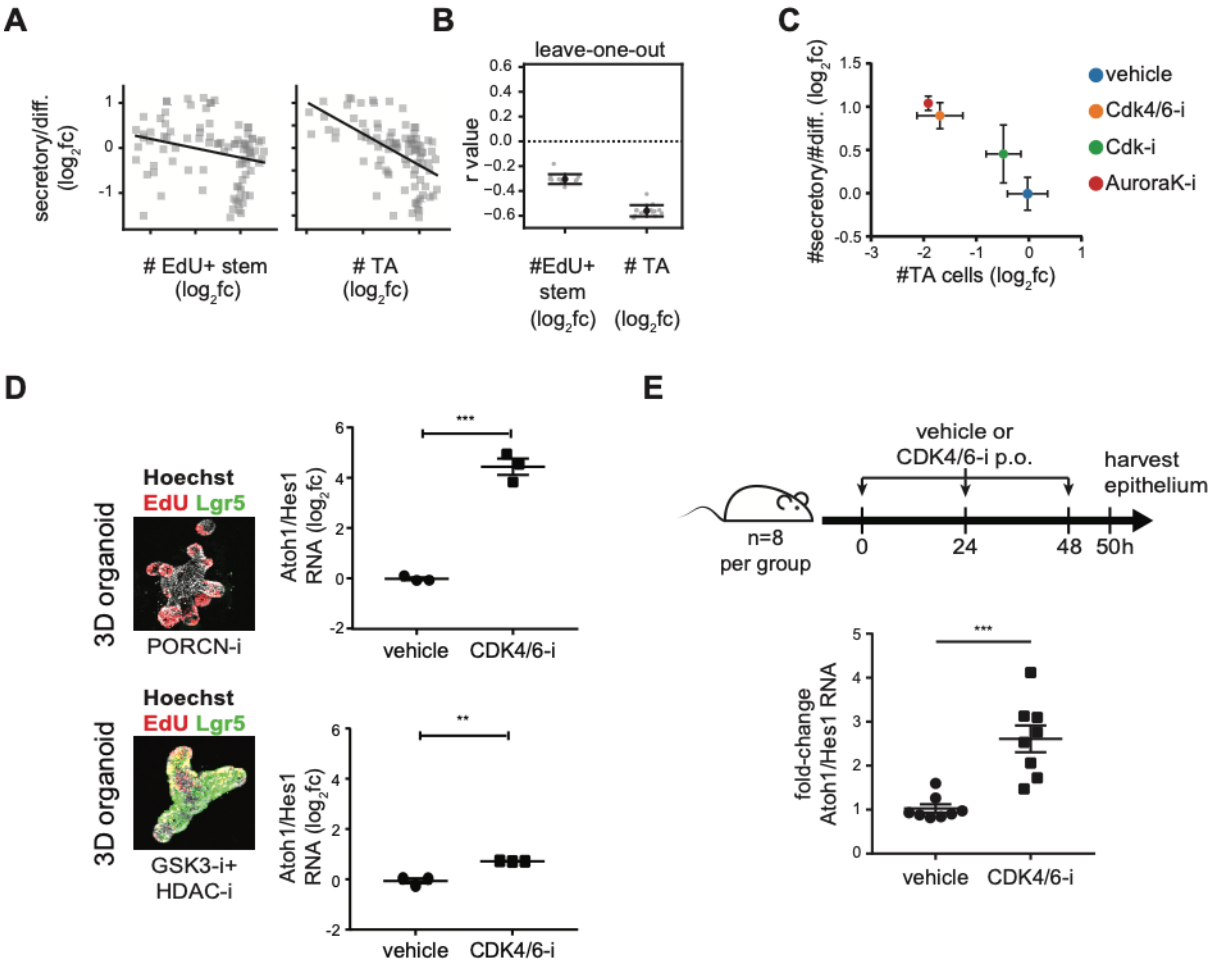

Figure 4. Inhibiting proliferation increases secretory cell prevalence in enteroid monolayers, in 3D organoids, and *in vivo*. (**A**) Numbers of transit-amplifying (TA) cells, but not EdU$^+$ stem cells, correlate with secretory cell fractions. Perturbation effects ($\log_2$fc) are plotted pairwise for each feature. (**B**) The TA-secretory correlation is not driven by a specific perturbation. Each of 13 perturbations was sequentially dropped from the dataset and r value calculated. (**C**) Inhibiting cell cycle progression increases secretory cell fractions. Enteroids were treated as indicated for 48hrs, after which #TA cells, and #secretory/#differentiated cells were quantified. n = 3 wells. (**D**) TA cells are sufficient to alter secretory fractions in response to cell cycle inhibitors. 3D organoids were perturbed into stem or TA cell-rich states using PORCN-i (TA) or GSK3-i+HDAC-i (stem), respectively. These factors were removed and then a CDK4/6

963 inhibitor (palbociclib) was applied. The secretory:absorptive ratio was measured at 2 days post-
964 treatment by qRT-PCR for the Atoh1/Hes1 ratio in TA-enriched (p=0.0002) or stem-enriched
965 (p=0.01) 3D organoids. n = 3 wells. (**E**) Impairing proliferation increases the
966 secretory:absorptive ratio *in vivo*. Mice were treated with CDK4/6-i (palbociclib) or vehicle
967 every 24hr for 48hrs. At 50hrs, intestinal crypts were harvested and gene expression was
968 measured by qRT-PCR. CDK4/6-i increases the Atoh1:Hes1 ratio (p=0.00005). n=8 mice/group.
969 Error bars mean +/- sem.

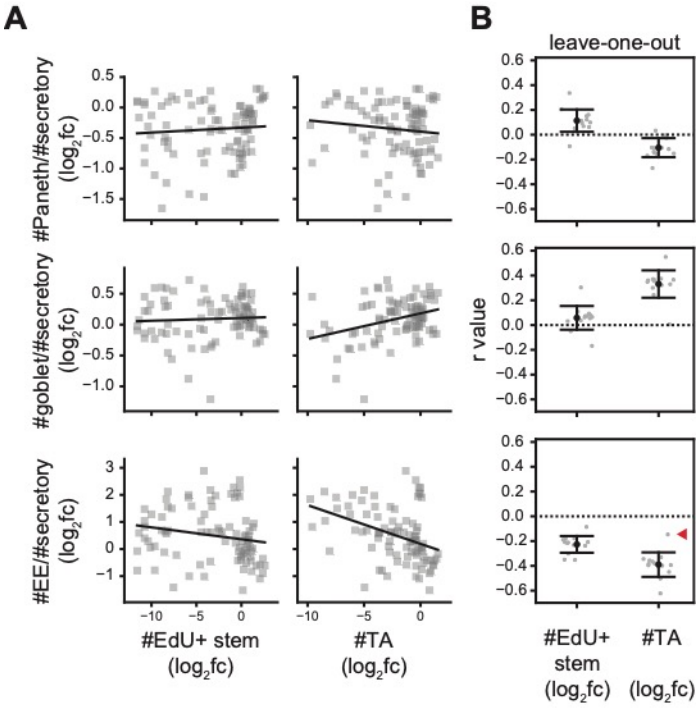

Figure 4-Supplement 1. The correlation between TA cell numbers and EE cell prevalence is driven by EGFR-i. (**A**) Numbers of transit-amplifying (TA) cells correlate with EE cell fractions. Perturbation effects (log_2fc) are plotted pairwise for each feature. (**B**) Each of 13 perturbations was sequentially dropped from the dataset and correlation coefficient (r value) calculated. Red arrowhead indicates loss of correlation between #TA cells and #EE/#secretory after dropping EGFR-i.

977 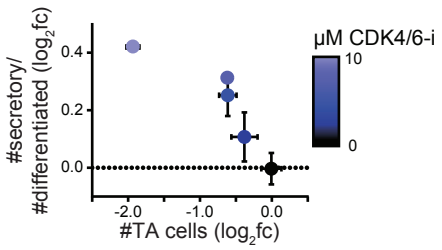

978 **Figure 4-Supplement 2. Dose-dependent increase in secretory prevalence upon CDK4/6**
979 **inhibition.** Increasing amounts of CDK4/6 inhibitor were applied (concentrations indicated by
980 color bar) to enteroid monolayers for 48 hours. Changes in the TA cells (#TA cells log_2fc) and
981 secretory cell prevalence amongst differentiated cells (#secretory/#differentiated log_2fc) were
982 quantified. The color of each point indicates the concentration of CDK4/6 inhibitor applied. n=3
983 wells.

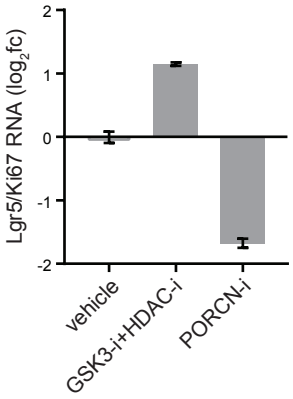

984

985 **Figure 4-Supplement 3. Confirming enrichment of stem versus proliferating cells in 3D**

986 **organoids treated with GSK3-i+HDAC-i or PORCN-i.** 3D organoids were treated with

987 GSK3-i+HDAC-i for 2 days or PORCN-i for 1 day and relative abundance of stem (Lgr5) and

988 proliferating (Ki67) cell RNA was measured by qRT-PCR. GSK3-i+HDAC-i increases stemness

989 relative to proliferation and PORCN-i decreases stemness relative to proliferation. n=3 wells.

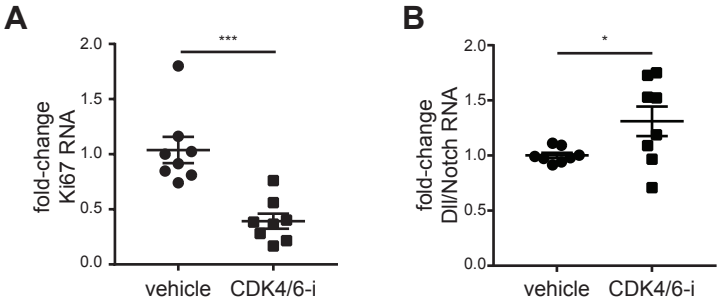

Figure 4-Supplement 4. Quantifying changes in proliferation and secretory prevalence in CDK4/6-i-treated mice. Small intestinal epithelial crypts were harvested from mice treated with vehicle or the CDK4/6-i palbociclib. (**A**) To quantify changes in proliferation, Ki67 RNA was measured by qRT-PCR. CDK4/6-i decreases Ki67 expression (p=0.0003). (**B**) To quantify changes in the ratio of secretory:absorptive cell-types, Dll (Dll1+Dll4) RNA and Notch (Notch1+Notch2) RNA was measured by qRT-PCR. CDK4/6-i increases the Dll/Notch ratio, indicating an increase in secretory cell-types (p=0.039). n=8 mice/group.

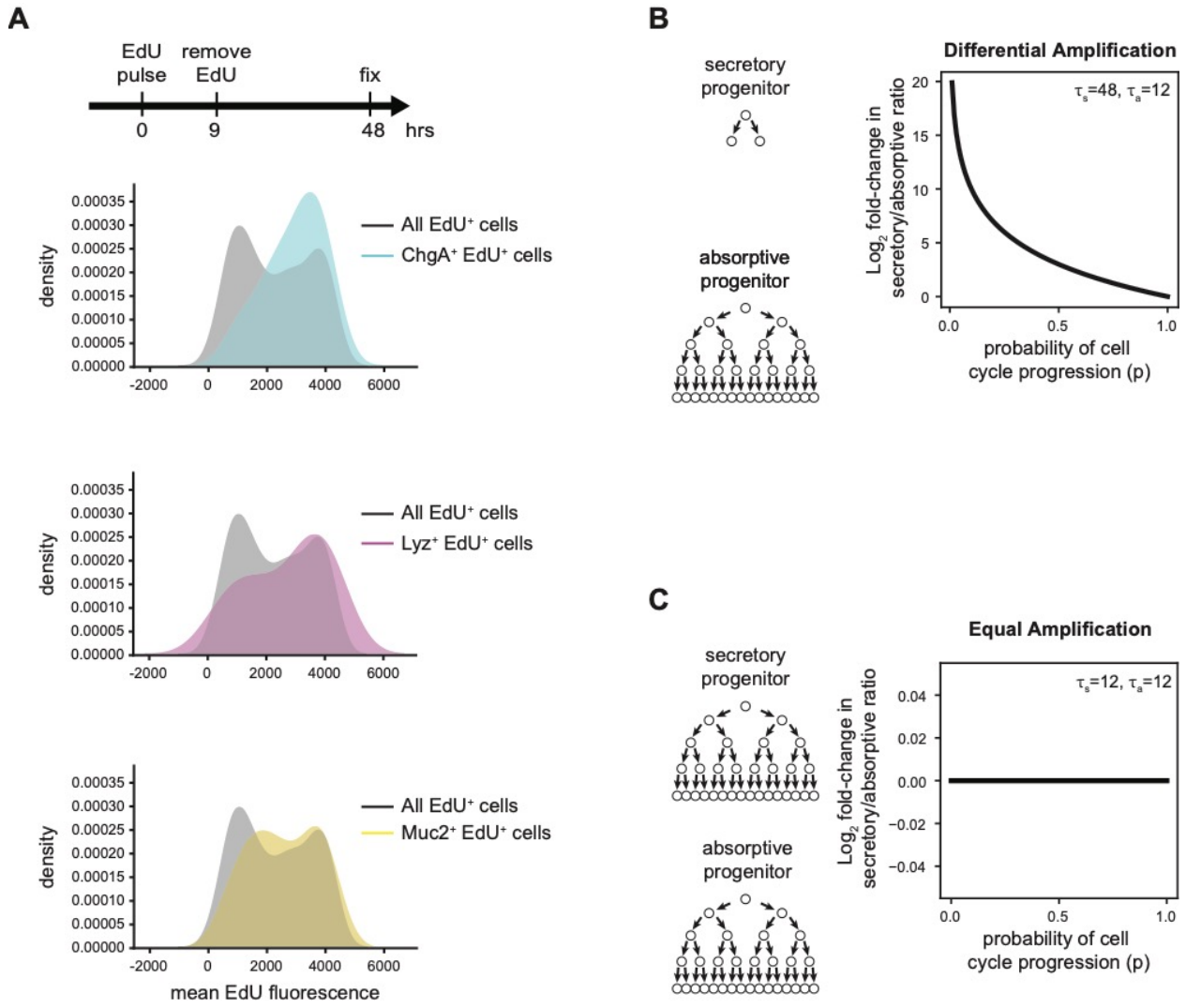

Figure 5. Differential amplification of secretory progenitors connects proliferation with differentiated cell-type composition. (**A**) Secretory progenitors divide fewer times than other progenitors. Enteroids were pulsed with EdU for 9 hours. After 39 further hours of culture enteroids were fixed and stained. Mean EdU signal intensity was quantified in all EdU$^+$ cells and in EdU$^+$ cells that also stained positive for markers of Paneth (Lyz), goblet (Muc2) and EE (ChgA) cells. Distribution of EdU intensities is represented as a kde plot. (**B**) If secretory progenitors divide fewer times than absorptive progenitors, inhibiting the cell cycle increases the secretory:absorptive ratio. Exponential growth model parameters are shown where secretory cell

1007 progenitors divide once (τ_s=48hr) and absorptive cell progenitors divide four times (τ_a=12hr)
1008 over a 48hr model time. (**C**) If secretory progenitors divide the same number of times as
1009 absorptive progenitors, inhibiting the cell cycle will not affect the secretory:absorptive ratio.
1010 Exponential growth model parameters are shown where both secretory and absorptive
1011 progenitors divide four times (τ_a=τ_s=12hr). For other model parameterizations see Figure 5-
1012 Supplement 1.

A

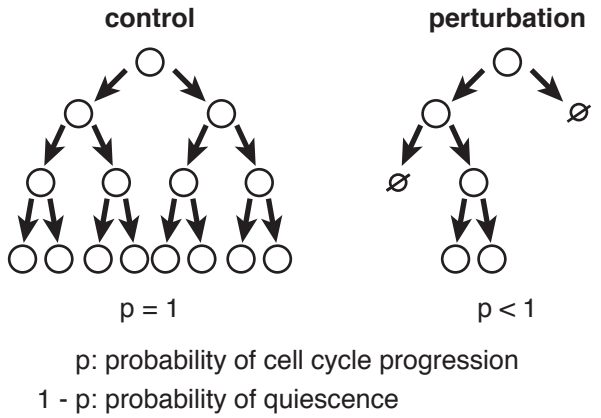
control
perturbation
p = 1
p < 1
p: probability of cell cycle progression
1 - p: probability of quiescence

B

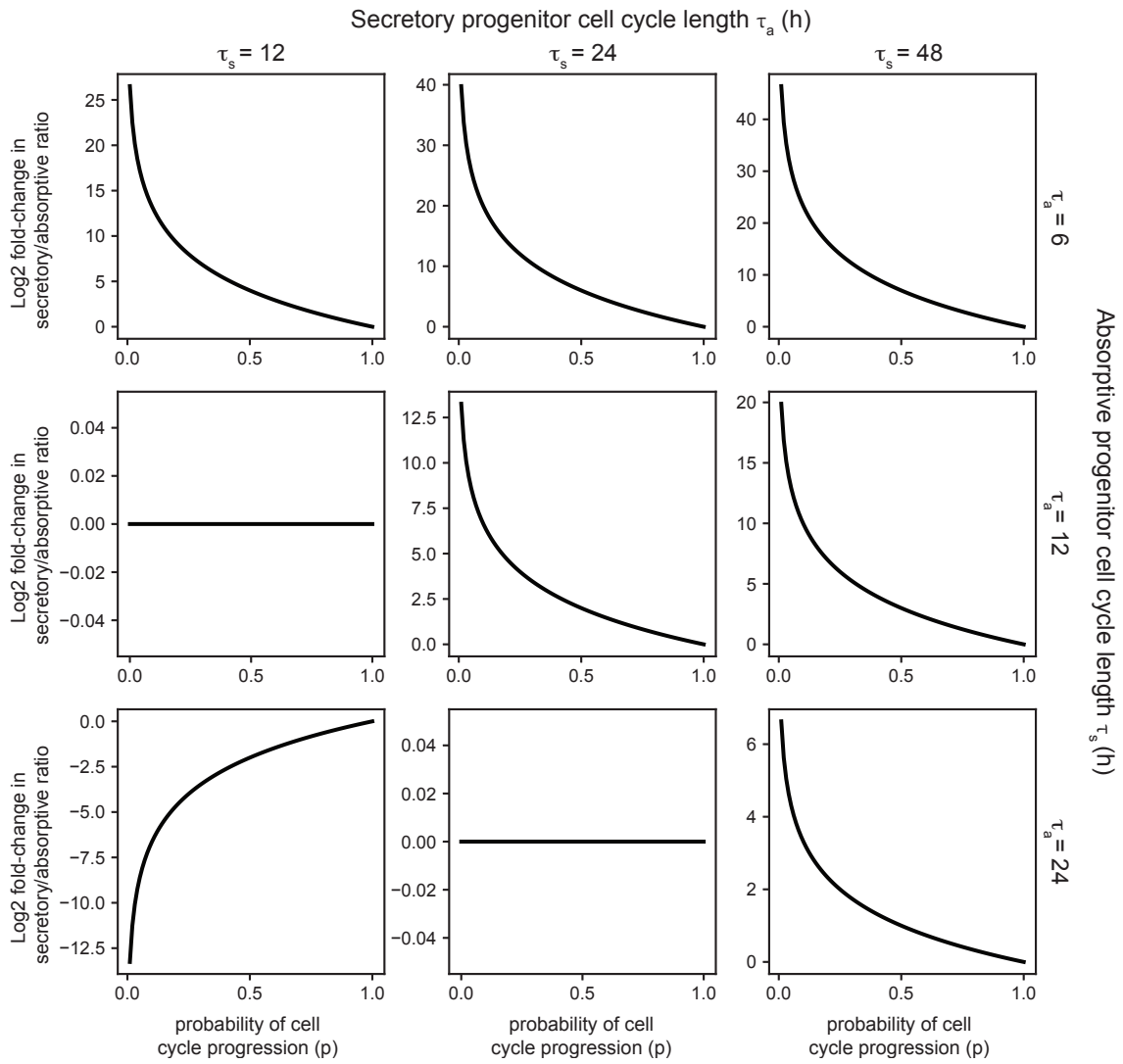
Secretory progenitor cell cycle length τ_a (h)
τ_s = 12
τ_s = 24
τ_s = 48
Absorptive progenitor cell cycle length τ_s (h)
τ_a = 6
τ_a = 12
τ_a = 24
Log2 fold-change in secretory/absorptive ratio
probability of cell cycle progression (p)

1013

1014 **Figure 5-Supplement 1. Cell cycle modulators affect the secretory:absorptive ratio due to**
1015 **differential amplification of secretory and absorptive progenitors.** (**A**) Diagram of the effect
1016 of altering p, a parameter setting the probability of progenitor cell cycle progression. (**B**)
1017 Exponential growth model supports the hypothesis that secretory progenitors divide fewer times
1018 than absorptive progenitors. The parameters τ_a and τ_s describe how often secretory and
1019 absorptive progenitors divide. Only when secretory progenitors have longer cell cycle lengths
1020 ($\tau_s > \tau_a$) and thus undergo fewer divisions than absorptive progenitors during the 48-hour
1021 simulation period does decreasing the probability of cell cycle progression increase the
1022 secretory:absorptive ratio, and vice versa.

1023 **Tables**

Cell-type	Marker	Precision	Recall	F1 Score
nuclei	Hoechst	0.9965	0.9936	0.9951
goblet cells	Muc2	1	0.8998	0.9473
EE cells	ChgA	0.8551	0.9248	0.8886
Paneth cells	Lyz	0.9018	0.9642	0.9319
EdU^+ cells	EdU	1	0.9557	0.9774
crypt regions	Lgr5-GFP	0.9816	0.9877	0.9846
stem cells	Lgr5-GFP	0.9724	0.9756	0.9740
$Lgr5^+/Dclk1^+$ cells	Lgr5-GFP	0.8208	0.9087	0.8625

1024 **Table 1.** Evaluation of the performance of cell-type identification algorithms.

Cell Type	*In Vivo* (%)	Enteroid Monolayer (%)
Paneth	7.5% of crypt cells(Cheng & Leblond, 1974a)	3.1% of all cells
Goblet	4-6(Cheng & Leblond, 1974a)	3.8
EE	0.6(Cheng & Leblond, 1974a)	0.4

1025 **Table 2.** Comparison of enteroid monolayer cell-type composition with literature reports of
1026 small intestine cell-type composition.

Pathway	Perturbation	Target	Designation	Pathway Effect	Published Effect(s) on Intestinal Epithelium	Dose Ref.
EGFR	erlotinib	EGFR	EGFR-i	inhibit	Reduced proliferation, increased EE cell (Basak et al., 2017a)	(Basak et al., 2017a)
Wnt	Wnt3a	Frizzled	Wnt3a	activate	Increased proliferation (Clevers, 2013)	(Thorne et al., 2018)
	IWP-2	PORCN	PORCN-i	inhibit	Decreased proliferation, stem cells, Paneth cells (Basak et al., 2017a; Farin et al., 2016; Rodríguez-Colman et al., 2017; van Es et al., 2005)	(Yin et al., 2014b)
	CHIR99021	GSK3	GSK3-i	activate	Increased proliferation, stem cells (Yin et al., 2014b)	(Yin et al., 2014b)
BMP	BMP4	BMPR	BMP4	activate	Decreased proliferation and stem cells (Qi et al., 2017)	(Thorne et al., 2018)
	LDN-193189	ALK2/3	BMPR-i	inhibit	Increased proliferation and stem cells (Li et al., 2018)	(Thorne et al., 2018)
TGF-β	TGF-β	TGF-βR	TGF-β	activate	Important for differentiation in vivo (Flentjar et al., 2007; Li et al., 2018; van der Flier et al., 2009)	(Han et al., 2014)
	EW-7197	ALK4/5	TGF-βR-i	inhibit	?	(Hong et al., 2017)
Notch	DAPT	γ-secretase	Notch-i	inhibit	Increased secretory cell-types (VanDussen et al., 2012)	(Yin et al., 2014b)
IL-4-JAK	IL-4	IL-4R	IL-4	activate	Increased goblet cells (von Moltke et al., 2015)	(von Moltke et al., 2015)
	baricitinib	JAK1/2	JAK1/2-i	inhibit	Altered stem cell numbers (Batlle et al., 2002; Richmond et al., 2018b)	(Dames et al., 2015)
HDAC	valproic acid	HDAC1/2	HDAC-i	inhibit	Increased stem cells (von Moltke et al., 2015; Yin et al., 2014b)	(Yin et al., 2014b)
p38 MAPK	SB202190	p38 MAPK	p38 MAPK-i	inhibit	Increased proliferation (M. Houde et al., 2001; Sato et al., 2011)	(Sato et al., 2011)

1027 **Table 3.** Selection of cell-type perturbations for study. For each perturbation, the specific
1028 pathway and target are indicated, as is the expected effect on the pathway and tissue. Designation
1029 is the code with which the perturbation is referred to in figures and text.

	Downregulating		Upregulating	
	Perturbation	**Log_2fc**	**Perturbation**	**Log_2fc**
EdU+ stem number	BMP4 + JAK1/2-i	-11.380	GSK3-i + p38 MAPK-i	2.602
	BMP4	-11.080	GSK3-i + JAK1/2-i	2.405
	BMP4 + Wnt3a	-10.380	BMPR-i + p38 MAPK-i	2.363
TA number	EGFR-i + HDAC-i	-9.476	GSK3-i + Wnt3a	1.541
	IL-4 + PORCN-i	-9.437	GSK3-i + JAK1/2-i	1.415
	EGFR-i + TGF-βR-i	-8.512	BMPR-i + Wnt3a	1.240
Secretory fraction (of differentiated cells)	TGFβ + Wnt3a	-1.544	GSK3-i + EGFR-i	1.109
	BMP4 + TGFβ	-1.509	EGFR-i + BMPR-i	1.096
	TGFβ + HDAC-i	-1.452	EGFR-i + JAK1/2-i	1.062
Paneth fraction (of secretory cells)	IL-4 + TGF-β	-1.651	BMPR-i + HDAC-i	0.307
	PORCN-i + TGF-β	-1.466	GSK3-i + HDAC-i	0.305
	IL-4 + p38 MAPK-i	-1.417	EGFR-i + TGF-β	0.270
Goblet fraction (of secretory cells)	EGFR-i + TGF-β	-1.209	IL-4 + p38 MAPK-i	0.724
	Notch-i + EGFR-i	-0.880	TGF-βR-i + Wnt3a	0.611
	EGFR-i + PORCN-i	-0.558	IL-4 + TGF-β	0.604
EE fraction (of secretory cells)	TGF-βR-i + Wnt3a	-1.525	PORCN-i + TGF-β	2.885
	IL-4 + HDAC-i	-1.419	Notch-i + TGF-β	2.542
	GSK3-i + HDAC-i	-1.098	TGF-β	2.282

1030 **Table 4.** Top perturbations in modulating cell-type composition.